



Finite-difference numerical modelling of gravito-acoustic wave propagation in a windy and attenuating atmosphere

Quentin Brissaud, Roland Martin, Raphael Garcia, Dimitri Komatitsch

► To cite this version:

Quentin Brissaud, Roland Martin, Raphael Garcia, Dimitri Komatitsch. Finite-difference numerical modelling of gravito-acoustic wave propagation in a windy and attenuating atmosphere. *Geophysical Journal International*, 2016, 206 (1), pp.308-327. 10.1093/gji/ggw121 . hal-01295427

HAL Id: hal-01295427

<https://hal.science/hal-01295427>

Submitted on 30 Mar 2016

HAL is a multi-disciplinary open access archive for the deposit and dissemination of scientific research documents, whether they are published or not. The documents may come from teaching and research institutions in France or abroad, or from public or private research centers.

L'archive ouverte pluridisciplinaire **HAL**, est destinée au dépôt et à la diffusion de documents scientifiques de niveau recherche, publiés ou non, émanant des établissements d'enseignement et de recherche français ou étrangers, des laboratoires publics ou privés.

Finite-difference numerical modelling of gravito-acoustic wave propagation in a windy and attenuating atmosphere

Quentin Brissaud¹, Roland Martin², Raphaël F. Garcia¹, Dimitri Komatitsch³

¹ *Institut Supérieur de l'Aéronautique et de l'Espace (ISAE-SUPAERO),*

Université de Toulouse, 31055 Toulouse cedex 4, France

² *Laboratoire de Géosciences Environnement Toulouse GET, UMR CNRS 5563, Observatoire Midi-Pyrénées, Université Paul Sabatier, 14 avenue Édouard Belin, 31400 Toulouse, France*

³ *LMA, CNRS UPR 7051, Aix-Marseille University, Centrale Marseille, 13453 Marseille cedex 13, France*

25 February 2016

SUMMARY

Acoustic and gravity waves propagating in planetary atmospheres have been studied intensively as markers of specific phenomena such as tectonic events or explosions or as contributors to atmosphere dynamics. To get a better understanding of the physics behind these dynamic processes, both acoustic and gravity waves propagation should be modelled in a 3D attenuating and windy atmosphere extending from the ground to the upper thermosphere. Thus, in order to provide an efficient numerical tool at the regional or global scale we introduce a finite difference in the time domain (FDTD) approach that relies on the linearized compressible Navier-Stokes equations with a background flow (wind). One significant benefit of such a method is its versatility because it handles both acoustic and gravity waves in the same simulation, which enables one to observe interactions between them. Simulations can be performed for 2D or 3D realistic cases such as tsunamis in a full MSISE-00 atmosphere or gravity-wave generation by atmospheric explosions. We validate the computations by comparing them to analytical solutions based on dispersion relations in specific benchmark cases: an atmospheric explosion, and a ground displacement forcing.

Key words: Acoustic-gravity waves – Wave propagation – Computational seismology – Numerical solutions – Tsunamis – Earthquake ground motions

1 INTRODUCTION

Propagation of acoustic and gravity waves in the atmosphere of planets has a wide range of scientific interests, from the interplay between these waves and atmosphere dynamics to the detection of tectonic events. Historically, this research topic was initially supported by ground-based observations of atmospheric infrasounds (see Le Pichon et al. (2010) for a review) and observations of thermospheric gravity waves through air-glow measurements, or electron content variations in the ionosphere (Hines 1960). Over the past twenty years the development of new observation tools allowing to recover electron density variations in the ionosphere (such as GNSS receivers located on the ground or in satellites, ionosondes, over-the-horizon and incoherent scattering radars...) has enabled the study of additional phenomena such as the emission of infrasounds by seismic surface waves or volcanic eruptions, as well as the emission of gravity waves by tsunamis or by large-scale atmospheric disturbances. Understanding these physical processes required the development of new tools capable of modelling wave propagation from the ground to the upper thermosphere (Lognonné et al. 1998; Occhipinti et al. 2006), and coupling with the ionosphere (Kherani et al. 2009). Recently, new types of observations based on air-glow emissions (Makela et al. 2011; Garcia et al. 2009) or in-situ measurements of air density in very low Earth-orbit satellites (Garcia et al. 2013, 2014) have provided respectively an increase of space/time coverage and resolution. Making optimal use of such improved precision and resolution in observations requires more sophisticated and accurate modelling tools. Thus, the propagation of both acoustic and gravity waves should be studied in a windy three-dimensional atmosphere model, including the thermosphere.

In order to provide realistic modelling at the regional or the global scale, physical simulations should include effects of attenuation, heterogeneous and realistic atmosphere models and strong wind perturbations. In this article we present a first

step towards this complex goal through the modelling of acoustic and gravity wave propagation in a planetary atmosphere based on a finite-difference numerical technique.

In a fluid two main approaches can be used, one based on a linearization of the full Navier-Stokes equations (Nappo 2002) and another one based on a decomposition of the gravito-acoustic equations in terms of potentials (Chaljub 2000). A third one, the full Navier-Stokes equations embedding non-linearities is also sometimes used (e.g for shock capturing or the study of turbulence) for atmospheric applications. In the context of non-linearities, Lecoanet et al. (2015) studied gravity wave generated by interface or Reynolds stress forcing in a coupled ocean/atmosphere model. Taking into account non-linearities they solved the 2D incompressible Navier-Stokes equations in a Fourier domain along x and over a Chebyshev grid along z . Wilson et al. (2004) studied 3D acoustic inviscid wave propagation based on finite differences and included turbulence and wind in their modelling. They provided a tool to study scattering phenomena affecting atmospheric remote-sensing systems. Finally, Snively & Pasko (2008) solved 2D Navier-Stokes equations for gravity waves with both wind and viscosity based on a finite volume method and focused on ducted gravity waves in the lower thermosphere. Another approach called the General Circulation Model (GCM), based on the compressible Navier-Stokes equations taking into account the Coriolis force but without gravity, gives interesting results about gravity wave propagation in a windy atmosphere (Miyoshi et al. 2014).

In the potential formulation, one makes the time evolution of the perturbations derive from a displacement potential and a gravity potential. In the presence of bulk attenuation only, such a decomposition into potentials can easily be applied (Chaljub 2000). but in the presence of deviatoric stress and/or of wind, this field representation is not valid any more because the potentials will not fully describe the solution of the Navier-Stokes equations (Valette 1987).

In this work we thus use the acoustic and advection parts of the compressible and viscous linearized version of the Navier-Stokes equations. As we will see below this system of equations allows one to couple gravity, wind velocity effects and acoustic wave propagation in the same unified numerical framework. Accuracy and limitations of the linear approximation were studied by Dörnbrack & Nappo (1997) by comparing the results of a linear model with a nonlinear, time-dependent, hydrodynamic numerical model. They pointed out that similar results are obtained from linear and non-linear models for wave stress, wave breaking height and wave dissipation through the critical level (Nappo 2002).

Linearization of the Navier-Stokes equations has been proposed by different authors: de Groot-Hedlin et al. (2011) resorted to a 2D finite-difference discretization but focused only on acoustic waves for realistic atmosphere models with wind and sound speed gradients. Ostashev et al. (2005) used the same discretization and considered 2D gravity waves but without atmospheric viscosity. Both articles considered atmospheric sources only. Mikhailenko & Mikhailov (2014) relied on 2D Laguerre/Fourier discretization to study low-altitude inviscid gravity waves in simple atmosphere models. Finally, Wei et al. (2015) focused on the tropopause and inviscid gravito-acoustic waves in the low atmosphere by means of a spectral/Laplace method. That study used a ground forcing technique in order to model tsunami-induced gravity waves: however to our knowledge acoustic-gravity wave propagation with stratified profiles of wind and strongly varying density, sound speed and viscosity has never been implemented in 3D.

Atmospheric attenuation is crucial for realistic simulations. Landau & Lifshitz (1959), Coulouvrat (2012) and Godin (2014) have established a formulation of the dynamic and volume viscosities and also developed analytical solutions for the evolution of pressure in the frequency domain in the presence of bulk and/or shear viscosity. In our simulations we will take into account both processes and their fluctuations through altitude because attenuation parameters vary strongly owing to the drastic density decrease when altitude increases (Godin 2014).

In terms of numerical implementation, for spatial discretization we will use a classical staggered grid (Yee 1966; Madariaga 1976) because it provides an efficient and stable way of reaching high order for the discretization. This grid is widely used for wave propagation in solid and fluid media (Graves 1996; Chaljub et al. 2007) but to our knowledge the fourth-order implementation has not been used before for atmospheric studies. Another version of a staggered grid for the atmosphere has been used in Ostashev et al. (2005) and de Groot-Hedlin et al. (2011) in particular to treat advection terms. Contrary to these articles, here we perform the implementation of advection terms through upwind (non-centered backward/forward) schemes (Ferziger & Peric 2012) to take into account wind velocities of different signs and to avoid possible stability issues, mainly at outgoing boundaries. We will validate our numerical technique by making comparisons with analytical solutions derived for benchmark cases for the different physical features involved.

In this article, we first recall the governing equations, including their linearization and decomposition in terms of wind advective components and propagative perturbation components (acoustic and gravity waves). We then describe the wave attenuation parameters and link them to the parameters usually used in the acoustic and geophysics communities. We also introduce the finite-difference numerical implementation and validate the 2D code by performing comparisons to analytical solutions in simplified atmosphere models. We present examples of 2D applications for atmosphere bottom forcing by tsunamis and by seismic waves, and then for atmospheric explosions in realistic atmosphere models. We finally validate the 3D code by performing comparisons to analytical solutions in simplified atmosphere models.

2 LINEAR GRAVITO-ACOUSTIC PROPAGATION IN A WINDY, ABSORPTIVE MEDIUM STABLY STRATIFIED

2.1 Governing equations

In this section we recall how the Eulerian form of the equations of motion is derived from the Eulerian momentum, mass conservation and state equations. One starts from the conservation of energy (Vallis 2006)

$$D_t I = D_t Q - P D_t (1/\rho_T), \quad (1)$$

where $D_t = \partial_t + \mathbf{V} \cdot \nabla$ denotes the Lagrangian derivative, I is the internal energy, Q is the heat input to the body, P the pressure, and ρ_T the atmospheric density. From the Eulerian formulation of the momentum equation (Landau & Lifshitz 1959),

$$\rho_T D_t \mathbf{V} - \nabla \cdot \boldsymbol{\Sigma}_T = \mathcal{F}_{ext} = \rho_T \mathbf{G}, \quad (2)$$

in which \mathbf{V} is the velocity, $\boldsymbol{\Sigma}_T$ the Eulerian stress tensor and \mathcal{F}_{ext} an external volumic force, equal to gravity forces in our case, where \mathbf{G} is the gravitational acceleration, and from the mass conservation equation

$$D_t \rho_T = -\rho_T \nabla \cdot \mathbf{V} \quad (3)$$

the following assumptions are then made:

- (i) The atmosphere is considered as a Newtonian fluid. Thus in the Eulerian description, the stress tensor reads

$$(\boldsymbol{\Sigma}_T)_{ij} = -P\delta_{ij} + (\boldsymbol{\Sigma}'_T)_{ij}, \quad (4)$$

where P is the pressure, $\boldsymbol{\Sigma}'_T$ is the viscous stress tensor and δ the Kronecker symbol.

- (ii) The atmosphere is considered as an ideal gas

$$dI = C_\nu dT \text{ and } P = \rho_T R T, \quad (5)$$

where P is the pressure, $R = C_p - C_\nu$ the gas constant, C_ν the heat capacity at constant volume, C_p the heat capacity at constant pressure, T the temperature and ρ_T the atmospheric density.

- (iii) State variables can be split into a stationary component (subscript 0) and a small space/time variable component (subscript 1) :

$$P = P_0 + P_1; \rho_T = \rho_0 + \rho_1; \mathbf{G} = \mathbf{G}_0 + \mathbf{G}_1; \mathbf{U} = \mathbf{U}_0 + \mathbf{U}_1; \mathbf{V} = \mathbf{V}_0 + \mathbf{V}_1; \boldsymbol{\Sigma}_T = \boldsymbol{\Sigma}_0 + \boldsymbol{\Sigma}_1 \quad (6)$$

where $P, \rho_T, \mathbf{G}, \mathbf{U}, \mathbf{V}$ are respectively the pressure, atmospheric density, gravitational acceleration, displacement and velocity.

- (iv) The atmosphere is stratified and thus physical parameters $\rho_0, \mathbf{G}_0, \eta_V, \mu, \mathbf{V}_0$ (respectively the atmospheric density, volume viscosity, dynamic viscosity and wind velocity) only vary along z .
- (v) The background velocity \mathbf{V}_0 is a stationary stratified horizontal wind, i.e., $\mathbf{V}_0(\mathbf{x}) = V_{0,x}(z) \cdot \mathbf{e}_x + V_{0,y}(z) \cdot \mathbf{e}_y$, where $\mathbf{x} = (x, y, z)$. This assumption will lead to a divergence-free wind ($\nabla \cdot \mathbf{V}_0 = 0$) and remove the influence of background wind on the hydrostatic equilibrium specified in assumption (vi).
- (vi) The hydrostatic equilibrium is considered as a reference state

$$\boldsymbol{\Sigma}_0 = -P_0 \mathbf{I}_d \quad (7)$$

with $\boldsymbol{\Sigma}_0$ the reference state tensor, P_0 the background pressure and \mathbf{I}_d the identity tensor in \mathbb{R}^3 . By assuming that the initial atmosphere is stratified and at hydrostatic equilibrium (2) one can formulate an equation describing this initial state as

$$\nabla \cdot \boldsymbol{\Sigma}_0 + \rho_0 \mathbf{G}_0 = 0. \quad (8)$$

By injecting (7) into (8) one obtains

$$\rho_0 \mathbf{G}_0 = \nabla P_0. \quad (9)$$

- (vii) We will make a linear assumption, i.e., we will neglect second-order terms by removing the $O(\mathbf{u}^2)$ terms.
- (viii) The wave perturbations are considered close to the adiabatic condition: $D_t Q = 0$.
- (ix) One makes the Cowling approximation (Cowling 1941) for the gravitational field. It consists in ignoring perturbations in the gravitational field, such that

$$\rho_T \mathbf{G} = \rho_0 \mathbf{G}_0 + \rho_1 \mathbf{G}_0. \quad (10)$$

- (x) We consider a regional scale domain and neglect the Coriolis force.

Hypothesis (ii) can be recast in a more convenient form

$$D_t I = C_\nu D_t T \text{ and } T = \frac{P}{\rho_T R} \Leftrightarrow D_t I = \frac{C_\nu}{R} D_t (P/\rho_T). \quad (11)$$

Injecting it into the energy conservation equation (1) and taking into account the adiabatic condition (viii) with P_a being the adiabatic pressure, this yields

$$\begin{aligned} \frac{C_p}{R} D_t \left(\frac{P_a}{\rho_T} \right) &= -P D_t (1/\rho_T) \\ \frac{C_p}{R} [(1/\rho_T) D_t P_a + P_a D_t (1/\rho_T)] &= -P_a D_t (1/\rho_T) \\ \frac{C_p}{R} [(1/\rho_T) D_t P_a - P_a D_t \rho_T / \rho_T^2] &= P_a D_t \rho_T / \rho_T^2 \\ D_t P_a &= P_a \frac{D_t \rho_T}{\rho_T} \left(\frac{R}{C_p} + 1 \right). \end{aligned} \quad (12)$$

Since we used the adiabatic assumption to get equation (12), we will only work with the adiabatic pressure P_a . Thenceforth, we will use the notation $P = P_a$, where P will refer to the adiabatic pressure.

Combining this with the mass conservation equation (3) yields

$$D_t P = -P \gamma \nabla \cdot \mathbf{V} \quad (13)$$

where $\gamma = \frac{C_p}{C_v}$ is the specific heat ratio.

One then gets a coupled system of equations: the pressure evolution equation (13) and the Eulerian form of the momentum equation (2) (details can be found in Vallis (2006) and Chaljub (2000)):

$$\begin{aligned} D_t P &= -P \gamma \nabla \cdot \mathbf{V} \\ \rho_T D_t \mathbf{V} - \nabla \cdot \boldsymbol{\Sigma}_T &= \rho_T \mathbf{G}. \end{aligned} \quad (14)$$

Unknowns are then split into ambient and perturbation values (iii), and from the linear hypothesis (vii), the reference state considered (vi) and the Cowling approximation (ix), eq. (14)-1 then reads (see e.g. Chaljub (2000))

$$\begin{aligned} \partial_t P_1 + (\mathbf{V}_0 + \mathbf{V}_1) \nabla (P_0 + P_1) &= -(P_0 + P_1) \gamma \nabla \cdot \mathbf{V}_1 \\ \partial_t P_1 &= -\mathbf{V}_0 \cdot \nabla P_1 - \rho_0 c^2 \nabla \cdot \mathbf{V}_1 - \rho_0 \mathbf{V}_1 \cdot \mathbf{G}_0, \end{aligned} \quad (15)$$

where c is the adiabatic sound speed

$$c = \left(\gamma \frac{P_0}{\rho_0} \right)^{1/2}. \quad (16)$$

Splitting the mass conservation equation (3) into ambient and perturbation values according to (iii) yields

$$\begin{aligned} D_t \rho_T &= -\rho_T \nabla \cdot \mathbf{V} \\ \partial_t \rho_T &= -\nabla \cdot (\rho_T \mathbf{V}) \\ \partial_t \rho_1 &= -\nabla \cdot (\mathbf{V}_0 \rho_0 + \mathbf{V}_0 \rho_1 + \mathbf{V}_1 \rho_0 + \mathbf{V}_1 \rho_1). \end{aligned} \quad (17)$$

Considering the divergence-free background wind (v) and the linear assumption (vii) one then has

$$\begin{aligned} \partial_t \rho_1 &= -\nabla \cdot (\mathbf{V}_0 \rho_1 + \mathbf{V}_1 \rho_0) \\ \partial_t \rho_1 &= -\nabla \rho_1 \cdot \mathbf{V}_0 - \nabla \cdot (\mathbf{V}_1 \rho_0). \end{aligned} \quad (18)$$

Now turning to the momentum equation, considering the divergence-free background wind (v) and the linear assumption (vii), (14)-2 reads

$$\begin{aligned} \rho_T D_t \mathbf{V} &= \nabla \cdot \boldsymbol{\Sigma}_T + \rho_T \mathbf{G} \\ \rho_0 \partial_t \mathbf{V}_1 + \rho_0 \{ (\mathbf{V}_1 \cdot \nabla) \mathbf{V}_0 + (\mathbf{V}_0 \cdot \nabla) \mathbf{V}_1 \} &= \nabla \cdot \boldsymbol{\Sigma}_1 + \nabla \cdot \boldsymbol{\Sigma}_0 - \mathbf{G}_0 \rho_1 - \mathbf{G}_0 \rho_0. \end{aligned} \quad (19)$$

Combined with the static equilibrium equation (8) this yields

$$\rho_0 \partial_t \mathbf{V}_1 = -\rho_0 \{ (\mathbf{V}_1 \cdot \nabla) \mathbf{V}_0 + (\mathbf{V}_0 \cdot \nabla) \mathbf{V}_1 \} + \nabla \cdot \boldsymbol{\Sigma}_1 + \mathbf{G}_0 \rho_1. \quad (20)$$

Using (15), (18) and (20), the whole system (14) then reduces to:

$$\begin{aligned} \partial_t P_1 &= -\mathbf{V}_0 \cdot \nabla P_1 - \rho_0 c^2 \nabla \cdot \mathbf{V}_1 - \rho_0 \mathbf{V}_1 \cdot \mathbf{G}_0 \\ \partial_t \rho_1 &= -\mathbf{V}_0 \cdot \nabla \rho_1 - \nabla \cdot (\rho_0 \mathbf{V}_1) \\ \rho_0 \partial_t \mathbf{V}_1 &= -\rho_0 \{ (\mathbf{V}_1 \cdot \nabla) \mathbf{V}_0 + (\mathbf{V}_0 \cdot \nabla) \mathbf{V}_1 \} + \nabla \cdot \boldsymbol{\Sigma}_1 + \mathbf{G}_0 \rho_1, \end{aligned} \quad (21)$$

where the stress tensor $\boldsymbol{\Sigma}_1$, under assumption (i), reads, $\forall (i, j) \in [1, 3] \times [1, 3]$

$$(\boldsymbol{\Sigma}_1)_{ij} = -P_1 \delta_{ij} + \mu (\partial_j V_i + \partial_i V_j - \frac{2}{3} \delta_{ij} \nabla \cdot \mathbf{V}) + \eta_V \delta_{ij} \nabla \cdot \mathbf{V}, \quad (22)$$

where δ is the Kronecker symbol.

To simplify the writing in what follows we will drop subscripts and write

$$\rho_0 = \rho; \rho_1 = \rho_p; \mathbf{G}_0 = \mathbf{g}; P_1 = p; \mathbf{V}_1 = \mathbf{v}; \mathbf{V}_0 = \mathbf{w}; \mathbf{U}_1 = \mathbf{u}; \boldsymbol{\Sigma}_1 = \boldsymbol{\Sigma}. \quad (23)$$

Eq. (21) then reads

$$\begin{aligned} \partial_t p &= -\mathbf{w} \cdot \nabla p - \rho c^2 \nabla \cdot \mathbf{v} - \rho \mathbf{v} \cdot \mathbf{g} \\ \partial_t \rho_p &= -\mathbf{w} \cdot \nabla \rho_p - \nabla \cdot (\rho \mathbf{v}) \\ \rho \partial_t \mathbf{v} &= -\rho \{ (\mathbf{v} \cdot \nabla) \mathbf{w} + (\mathbf{w} \cdot \nabla) \mathbf{v} \} + \nabla \cdot \boldsymbol{\Sigma} + \mathbf{g} \rho_p \end{aligned} \quad (24)$$

With these notations (23) the stress tensor Σ then reads, $\forall(i, j) \in [1, 3] \times [1, 3]$,

$$(\Sigma)_{ij} = -p\delta_{ij} + \mu(\partial_j(\mathbf{v} + \mathbf{w})_i + \partial_i(\mathbf{v} + \mathbf{w})_j - \frac{2}{3}\delta_{ij}\nabla \cdot \mathbf{v}) + \eta_V\delta_{ij}\nabla \cdot \mathbf{v}. \quad (25)$$

The system of equation (24) describes simultaneously the propagation of both acoustic and gravity waves in a viscous fluid subject to wind. Note that in order to establish eq. (24) we did not use the stratified atmosphere assumption (iv) for density, adiabatic sound speed, viscosity nor gravity but only for wind profiles. It means that any 3D varying profile of atmosphere can be considered for background parameters besides background wind. But in simulations presented later on in this paper, for validations or applications, we only considered stratified media since it enabled us to get simple analytical solutions. Expansion of (24) in component form can be found in Appendix A. In the remainder of the article we will refer by "wind-convective" terms to the following terms in (A.1):

- (a) $\mathbf{w} \cdot \nabla p, \mathbf{w} \cdot \nabla \rho_p$
- (b) $(\mathbf{w} \cdot \nabla) \mathbf{v}$
- (c) $(\mathbf{v} \cdot \nabla) \mathbf{w}$.

2.2 Atmospheric viscosity and acoustic attenuation

Atmospheric absorption can occur by two main mechanisms (Bass et al. 1984): classical losses due to dissipation of mechanical energy and relaxation losses due to the conduction of heat energy. The dynamic viscosity μ , due to shear stress applied to a fluid, reads (Zuckerwar & Ash 2006; Bass & Chambers 2001)

$$\mu = \frac{2}{3}L\rho c\sqrt{2/\pi\gamma}, \quad (26)$$

where L is the mean free path, c the adiabatic sound speed (16) and $\gamma = C_p/C_v$ the specific heat ratio. The volume viscosity η_V due to the relaxation of dilatational disturbances (i.e., heat conduction and molecular relaxations) reads

$$\eta_V = \frac{4}{3}\mu + \frac{(\gamma - 1)\kappa}{\gamma C_v}, \quad (27)$$

where μ is the dynamic viscosity, $\gamma = C_p/C_v$ the specific heat ratio, C_v the molar low-frequency specific heat at constant volume and κ the thermal conductivity. The acoustic absorption coefficient α (in m^{-1}) describes the frequency dependence of the attenuation process. This coefficient is the imaginary part of the wavenumber $k = \text{Re}(k) - i\alpha$ (Landau & Lifshitz 1959); From Bass & Chambers (2001) it writes

$$\alpha(f) = \frac{2(\pi f)^2}{\rho c^3}\eta_V. \quad (28)$$

When acoustic or seismic waves are modelled, Zener, Maxwell or Kelvin-Voigt are commonly used to introduce attenuation effects in the time domain (Moczo & Kristek (2005) show that several of these models are equivalent). Viscoelasticity in solids, modelled using the Zener model in the time domain, is introduced in the discretized equations through memory variables (Carcione 2014). Doing so avoids having to explicitly handle a convolution process with the whole past of the viscoelastic material, which is a complicated process from a numerical point of view (Carcione et al. 1988; Moczo 1989; Robertsson et al. 1994). But in the Earth atmosphere volume and dynamic viscosities tend to act as a Kelvin-Voigt viscoelastic mechanism. For a Kelvin-Voigt solid one can represent the absorption coefficient, which is proportional to the inverse of its quality factor, as a function of frequency. Using this formulation, we will show in a simple case that this choice of viscoelastic mechanism is reasonable by comparing its absorption coefficient to the theoretical one in (28).

We consider a simple homogeneous (i.e with constant density and sound velocity) atmosphere model in which the volume viscosity η_V is constant and the shear viscosity is not taken into account (for $i \neq j$, $\Sigma_{ij} = 0$). We also neglect background velocity ($\mathbf{w} = \mathbf{0}$) and gravitation ($\mathbf{g} = \mathbf{0}$). Eq. (24) then yields

$$\begin{aligned} \partial_t p &= -\rho c^2 \nabla \cdot \mathbf{v} \\ \partial_t \rho_p &= -\nabla \cdot (\rho \mathbf{v}) \\ \rho \partial_t \mathbf{v} &= \nabla \cdot \Sigma, \end{aligned} \quad (29)$$

where

$$\Sigma = (-p + \eta_V \nabla \cdot \mathbf{v}) \mathbf{I}_d, \quad (30)$$

\mathbf{I}_d being the identity tensor in \mathbb{R}^3 . After replacing the pressure term in Equation (29)-3 with the primitive of Equation (29)-1, one obtains the formulation of the stress-strain relationship for a Kelvin-Voigt solid, as described for instance by Carcione (2014), eq. (2.159):

$$(\Sigma)_{ij, 1 \leq i, j \leq 3} = (M_R \epsilon + \eta \dot{\epsilon}) \delta_{ij}, \quad (31)$$

where Σ is the stress tensor, $M_R = \rho c^2$ the bulk modulus, $\eta = \eta_V$ the bulk viscosity and ϵ the strain, defined from the

displacement \mathbf{u} by $\epsilon = \nabla \cdot \mathbf{u}$. Unknowns are assumed to be Fourier functions in time and space such that

$$\mathbf{u}(\mathbf{x}, t) = u_0 e^{i(\mathbf{k}\mathbf{x} - \omega t)}. \quad (32)$$

From (29) the dispersion relation in this case reads

$$k^2 \left(1 - \frac{i}{D}\right) - \left(\frac{\omega}{c}\right)^2 = 0, \quad (33)$$

where $D = \frac{\rho c^2}{w \eta_V}$, which yields

$$k^2 = \left(\frac{\omega}{c}\right)^2 \frac{(1 + \frac{i}{D})}{(1 + \frac{1}{D^2})}. \quad (34)$$

The quality factor then reads (Carcione et al. 1988)

$$Q = \frac{Re(k^2)}{Im(k^2)} = D = \frac{\rho c^2}{2\pi f \eta_V}. \quad (35)$$

One then gets the final dispersion relation by taking the square root of (34):

$$k = \frac{w}{\sqrt{2}c} \left\{ \frac{1}{1 + (1/Q)^2} + \frac{1}{[1 + (1/Q)^2]^{1/2}} \right\}^{1/2} + i \frac{w}{\sqrt{2}c} \left\{ \frac{1}{1 + (1/Q)^2} - \frac{1}{[1 + (1/Q)^2]^{1/2}} \right\}^{1/2}. \quad (36)$$

This expression enables one to compute both the phase velocity and the absorption coefficient. From Carcione (2014), the phase velocity reads

$$v_\phi = \frac{\omega}{Re(k)}, \quad (37)$$

where $Re(k)$ is the real part of the wavenumber k . Equation (36) then yields

$$v_\phi = \sqrt{2}c \left(\frac{1}{1 + (1/Q)^2} + \frac{1}{[1 + (1/Q)^2]^{1/2}} \right)^{-1/2}. \quad (38)$$

Considering altitudes below typically 400 km and low-frequency signals smaller than typically 1 Hz, it is reasonable to make the assumption $Q \gg 1$ and then to develop this expression to the second order in $\frac{1}{Q}$. Doing so the phase velocity (38) can then be written as

$$v_\phi \approx \frac{c}{1 - \frac{3}{8} \left(\frac{1}{Q}\right)^2}. \quad (39)$$

This expression is the one given by Blackstock (2000), page 306. Consequently, acoustic wave propagation in an attenuated medium with bulk viscosity follows the Kelvin-Voigt relation and is dispersive. However, the $(1/Q)^2$ term is usually ignored in acoustics because it is a second-order term in $1/Q$. The wavenumber reads $k = Re(k) - i\alpha$, where α is the absorption coefficient

$$\alpha^2 = - \left(\frac{\omega}{c}\right)^2 \frac{1}{2(1 + (1/Q)^2)} (1 - \sqrt{1 + (1/Q)^2}). \quad (40)$$

By a Taylor expansion when $Q \gg 1$, one then gets

$$\alpha \approx \left(\frac{\omega}{c}\right) \frac{1}{2Q} \quad (41)$$

$$\alpha \approx \frac{2(\pi f)^2}{\rho c^3} \eta_V. \quad (42)$$

The Kelvin-Voigt absorption coefficients α and Q can thus be defined in terms of volume viscosity and frequency according to formulas (35) and (42). This result has been extended by Godin (2014) to the full absorption process, choosing into account both shear and volume viscosities. Eq. (9) in Godin (2014) shows that the traditional choice of picking constant coefficients leads to substantial quantitative errors, and in the infrasound limit Eq. (12) in that article gives a similar result as (28). Finally, the background flow that causes the Doppler effect will shift the wave frequency and will thus impact its absorption. Variations of viscosity coefficients (μ and η_V) with altitude and background flows will be taken into account in our numerical simulations.

3 ATMOSPHERE MODELS

We will simulate wave propagation in several atmosphere models. We will first use simplified models for validation of our numerical technique with respect to analytical solutions. In these first models all atmospheric parameters will be set to constant values. We will then design an isothermal atmosphere model to test the stability of the calculations relative to the exponential density decrease in the atmosphere. We will finally build a more realistic atmosphere model from empirical atmosphere models with only vertical variations of the parameters.

| H (km) | g_z (m.s ⁻²) | c (m.s ⁻¹) | N^2 (rad ² .s ⁻²) | γ (no unit) | T (in °K) |
|----------|----------------------------|--------------------------|--|--------------------|-------------|
| 29 | -9.831 | 639.5 | 10^{-4} | 1.67 | 1000 |

Table 1. Constant parameters of the isothermal model: from left to right, scale height, gravity, sound speed, square of the Brunt-Väisälä frequency, ratio of calorific capacities, and temperature. Volumic mass and pressure at the surface are set respectively to 0.4083 kg.m^{-3} and 10^5 Pa . We use a constant molar mass of 28.96 g.mol^{-1} .

3.1 Isothermal model

In order to infer the validity of our computations relative to the exponential density decrease in the atmosphere, we first create an isothermal model. Air density and pressure decrease exponentially with a constant scale height, all other parameters being constant. The values of these constant parameters are representative of those observed in the thermosphere and are summarized in Table 1. The model is built assuming an ideal gas in hydrostatic equilibrium at constant temperature (Nappo 2002).

3.2 Realistic atmosphere model

In order to verify the stability of our calculations relative to realistic vertical variations of atmospheric parameters, we create a model that exhibits only vertical variations of the atmospheric parameters that are extracted from the MSISE-00 atmosphere model (Picone et al. 2002), and from the HWM93 atmospheric wind model (Hedin 1991) when atmospheric winds are included. The thermodynamic properties of the atmospheric compounds are extracted from the NIST web-book data base (<http://webbook.nist.gov/chemistry/>). We extracted a vertical profile of these atmospheric parameters for conditions corresponding to a surface point at latitude 36.5° , longitude 158.7° at 7:47:40 UTC on March 11, 2011. This space and time location corresponds to the coordinates of the crossing between the post-seismic infrasonic waves generated by the Tohoku earthquake in Japan and the GOCE satellite (Garcia et al. 2013). This vertical profile is extended in 2D and 3D by invariant

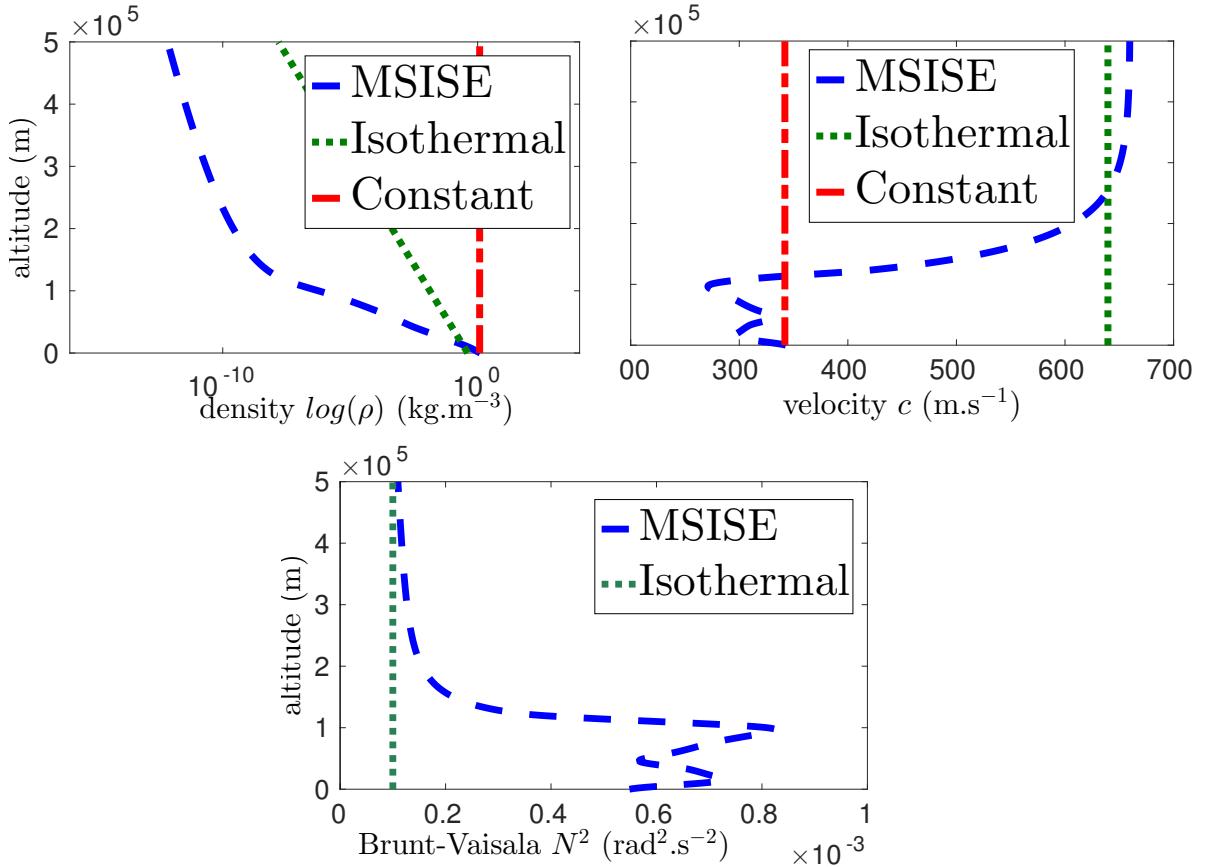
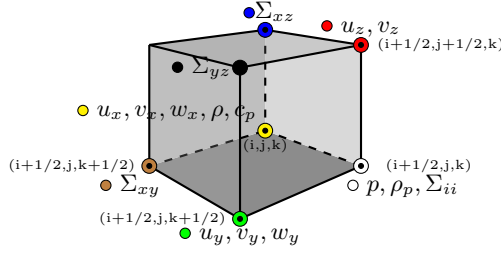


Figure 1. Vertical profiles of mean density, sound velocity and square of Brunt-Väisälä frequency extracted from empirical atmosphere model *MSISE* – 00 (Picone et al. 2002) and isothermal models in Table 1.

prolongation of the whole set of physical properties in the direction orthogonal to the 2D plane. Density, adiabatic sound speed and Brunt-Väisälä frequency versus altitude are presented in Figure 1. Other charts can be found in Appendix C.

4 NUMERICAL DISCRETIZATION

Time discretization is carried out based on a fourth-order Runge-Kutta scheme and spatial discretization is based on a fourth-order staggered scheme. We have performed comparisons, not shown here, that demonstrate that in our case there is no significant benefit of using a more sophisticated scheme such as a low-dissipation and low-dispersion fourth-order Runge-Kutta algorithm (LDDRK, Berland et al. (2006)). For spatial discretization we use the following stencil:



Stencil showing where unknowns are computed in the mesh. Colored circles in front of unknowns show to which node these unknowns depend.

For a scalar unknown u computed at time step m and at grid point (i, j, k)

$$u_m^{i,j,k} = u(i\Delta x, j\Delta y, k\Delta z, m\Delta t), \quad (43)$$

within the domain Ω the finite-difference operators read

$$\begin{aligned} (\partial_x u)_m^{(i,j,k)} &= \frac{27u_m^{(i+1,j,k)} - 27u_m^{(i,j,k)} - u_m^{(i+2,j,k)} + u_m^{(i-1,j,k)}}{24\Delta x} \\ (\partial_y u)_m^{(i,j,k)} &= \frac{27u_m^{(i,j,k)} - 27u_m^{(i,j-1,k)} - u_m^{(i,j+1,k)} + u_m^{(i,j-2,k)}}{24\Delta y} \\ (\partial_z u)_m^{(i,j,k)} &= \frac{27u_m^{(i,j,k)} - 27u_m^{(i,j,k-1)} - u_m^{(i,j,k+1)} + u_m^{(i,j,k-2)}}{24\Delta z}. \end{aligned} \quad (44)$$

Note that in Equation (24) the pressure and density perturbation evolution equations require the calculation of ∇p and $\nabla \rho_p$ at the same spatial location as, respectively, p and ρ_p , in term (a). We select a non-staggered upwind or downwind scheme depending on the sign of w_x in order to properly treat the advective terms (Ferziger & Peric 2012). The instability that can otherwise arise from a centered scheme comes from the fact that the flow goes from upstream to downstream and thus the derivative computed at any point should not take into account information downstream since it has no physical meaning. Similar instabilities appear when using the staggered grid described in (44). This upwind/downwind scheme writes:

$$\begin{aligned} \text{if } w_x < 0 \quad (\partial_x p)_m^{(i,j,k)} &= \frac{1}{6\Delta x} \{ 2(p_m^{(i,j,k)} - p_m^{(i-1,j,k)}) \\ &+ 6(p_m^{(i+1,j,k)} - p_m^{(i,j,k)}) - (p_m^{(i+2,j,k)} - p_m^{(i,j,k)}) \} \\ \text{if } w_x > 0 \quad (\partial_x p)_m^{(i,j,k)} &= \frac{1}{6\Delta x} \{ 2(p_m^{(i+1,j,k)} - p_m^{(i,j,k)}) \\ &+ 6(p_m^{(i,j,k)} - p_m^{(i-1,j,k)}) - (p_m^{(i,j,k)} - p_m^{(i-2,j,k)}) \} \end{aligned} \quad (45)$$

We apply the same kind of approach to other "wind-convective" terms involving $\rho_p, (v_x, v_y), w_x$, respectively in terms (a), (b)(c) and (c).

Note that other authors have used different staggered grids for spatial discretization. In order to choose the numerical method we implemented the spatial discretization presented in de Groot-Hedlin et al. (2011) coupled with the fourth-order Runge-Kutta scheme (in their publication they implemented a less accurate second-order scheme). It exhibited instabilities when performing various tests on atmospheric backgrounds with a strong wind (of about 100 m.s⁻¹) and a "high-frequency" wave generated by a point source (of about 5 s dominant time period). We thus choose to use the discretization (44)-(45) instead.

Regarding boundary conditions, we perform simulations in a simple Cartesian mesh in which $\Delta x = \Delta y = \Delta z$. On the left and right boundaries of the domain we implement periodic boundary conditions. This implies that the atmosphere model should be continuous between the right and left boundaries, which is the case since our models only vary along z . On the top edge of the grid, referred to as Γ_D , we enforce a homogeneous Dirichlet boundary condition that consists in imposing, at any time t , for $\mathbf{x} \in \Gamma_D$,

$$u(\mathbf{x}, t) = 0. \quad (46)$$

| $L_x \times L_z$ (km) | Δx (m) | Δt (s) | ρ | c | η_V | μ | g_z | w_x |
|-----------------------|----------------|----------------|---------|--------|----------|-------|--------|-------|
| 20×800 | 250 | 10^{-2} | varying | 652.82 | 0 | 0 | -9.831 | 0 |

Table 2. Simulation parameters for the isothermal model 3.1 without considering attenuation, used in Simulation 5.2, i.e., the case of a Bottom "high-frequency" forcing in a windless atmosphere with exponentially-decaying density and without attenuation. In this table we express parameters with the following dimensions: ρ (kg.m⁻³), c (m.s⁻¹), η_V (kg.m⁻¹.s⁻¹), μ (kg.m⁻¹.s⁻¹), g_z (m.s⁻²) and w_x (m.s⁻¹).

This choice has no real physical meaning but is implemented here for simplicity. It will lead to reflection when waves hit the boundary, but for large-enough meshes this choice has no measurable impact on signals observed. When simulating an atmospheric explosion, i.e. when the source is located inside the grid, we apply Dirichlet boundary conditions (46) on the bottom boundary as well.

In the other cases, i.e. when the seismic source is located outside the grid, we apply a forcing boundary condition along the bottom edge of the grid to simulate incoming seismic waves impinging from the bottom: at any time t , for $\mathbf{x} \in \Gamma_F$, for $f \in \mathbb{R}$

$$\mathbf{u}(\mathbf{x}, t) = \mathbf{f}(\mathbf{x}, t), \quad (47)$$

where \mathbf{f} is the forcing function.

At the edges of the computational grid, the discretization (44) requires the computation of unknown terms at position $j = 0, -1$. We compute these terms using a mirror condition, meaning that $\forall m, i, k$

$$p_m^{(i,0,k)} = 2p_m^{(i,1,k)} - p_m^{(i,2,k)} \quad (48)$$

which is the linear interpolation of $p_m^{(i,1,k)}$ from neighboring values $p_m^{(i,0,k)}, p_m^{(i,2,k)}$ expressed in terms of $p_m^{(i,0,k)}$. The same holds for $p_m^{(i,-1,k)}$, such that

$$p_m^{(i,-1,k)} = 2p_m^{(i,0,k)} - p_m^{(i,1,k)} \quad (49)$$

Since we will often perform simulations over large domains we resort to parallel computing implemented using the Message-Passing Interface (MPI) libraries (Gropp et al. 1994), decomposing the mesh into regular slices cut along the x -coordinate axis.

5 2D ACOUSTIC WAVE VALIDATION

5.1 Construction of the analytical solutions

We compute the analytical solution in the time domain for validation purposes for each test case using the following process:

- Calculation of the forcing signal for the whole time domain along the forcing boundary or at the point source,
- Calculation of the 3D (or 2D) Fourier transform (spatial and time transformations) of that function,
- Calculation of wavenumbers $k_x = 2\pi/\lambda_x$ and $k_y = 2\pi/\lambda_y$ for all spatial wavelengths $\lambda_{x,y}$
- Calculation of k_z from dispersion relations for all wavenumbers k_x, k_y and time frequencies (see Appendix B),
- Multiplication, in the Fourier domain, of the forcing function with a complex filter based on the representation of the solution in the case of an harmonic source or forcing term (see Appendix B for more details),
- Calculation of the inverse Fourier transform of the result at the recording stations to obtain the solution in the time domain.

5.2 Bottom "high-frequency" forcing in a windless atmosphere with exponentially-decaying density and without attenuation

The first validation step concerns acoustic waves and the underlying physical processes of dispersion and amplitude growth with altitude. We consider the following forcing function, $\forall \mathbf{x} \in \Gamma_F$:

$$f(\mathbf{x}, t) = e^{-\left[\frac{t-(t_0-P/4)}{P/4}\right]^2} - e^{-\left[\frac{t-(t_0+P/4)}{P/4}\right]^2}, \quad (50)$$

where P is the time period of the forcing signal and t_0 the starting forcing time. We set $P = 60$ s and $t_0 = 55$ s. The atmosphere is considered isothermal and described in Table 2.

Two particular features for atmospheric waves associated with density variations can be noticed in Figure 2: first, the amplification of vertical velocity/displacement amplitude due to the decrease of atmospheric density, since kinetic energy $E_c \propto \rho |\mathbf{v}|^2$ is conserved; second, the dispersion effect on the waveform. This latter point is due to the frequency dependence of phase velocity $v_p = v_p(\omega, c, H)$ (Landau & Lifshitz 1959).

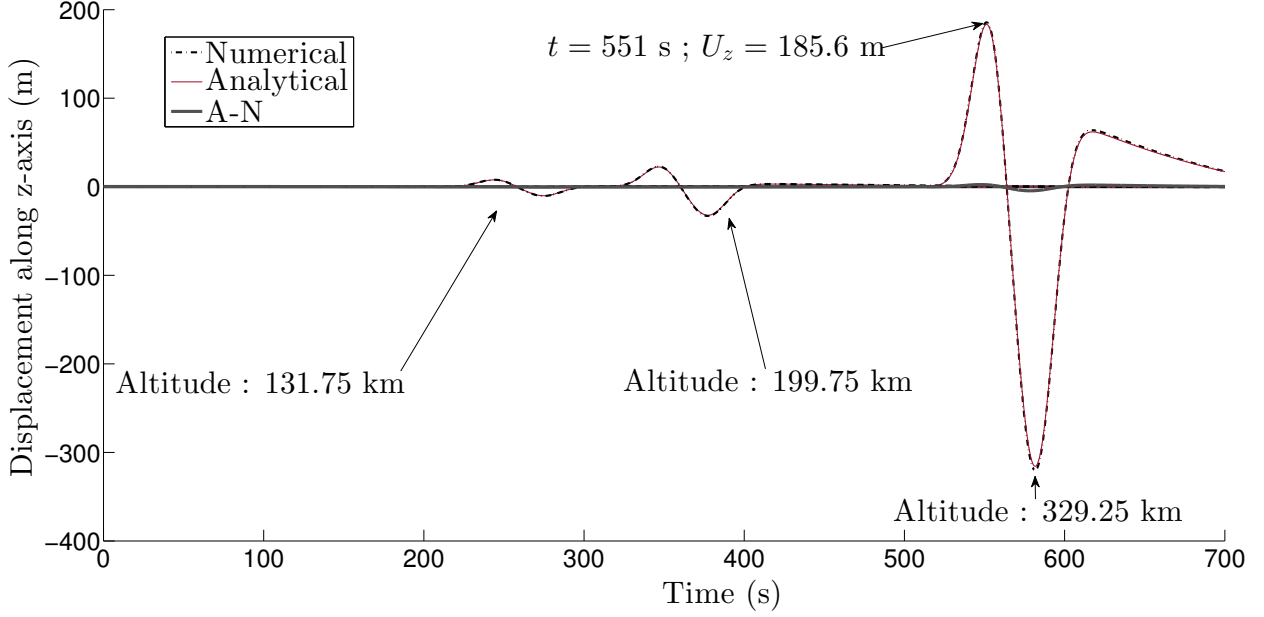


Figure 2. Vertical displacement for the finite-difference solution (‘Numerical’), the analytical solution (‘Analytical’) and the difference between the two (‘A-N’) through time for Simulation 5.2, i.e., the case of a Bottom “high-frequency” forcing in a windless atmosphere with exponentially-decaying density and without attenuation and for three recording stations located at altitudes $z = 131.75$, 199.75 and 329.25 km. The atmosphere is considered isothermal (Table 2).

5.3 Bottom “high-frequency” forcing in an attenuating, windless atmosphere with exponentially-decaying density

Here let us study and validate the effect of viscosity on acoustic waves. To do so in (50) we set $P = 15$ s and $t_0 = 30$ s. These parameters are slightly different from the previous case because the absorption coefficient α in (28) is frequency dependent and thus in order to clearly see its effect we need to select a frequency larger than in the previous case. The atmosphere is considered isothermal and described in Table 3.

Figure 3 shows a good fit between the analytical and numerical signals in terms of both wave amplitude and travel time, the error being less than 5% in maximum amplitude over time. Several physical phenomena can be observed: first, the decay in amplitude due to the atmospheric viscosity. In this case only the volumic viscosity impacts the propagation because acoustic (pressure) waves are not sensitive to shear stress. The other phenomenon is the apparent frequency dispersion, coming from the fact that the absorption coefficient (28) is frequency dependent and thus high frequencies are more attenuated than lower ones, which leads to a larger apparent period for the attenuated signal than for the non-attenuated one.

5.4 Atmospheric explosion in a windy homogeneous atmosphere

Here let us study and validate the effect of wind on acoustic waves. In this case we consider an atmospheric explosion, i.e. a sudden increase in volume inserted into the pressure equation, such that

$$\begin{aligned} Q &= \frac{-2\pi}{P}(t - t_0)e^{-\left[\frac{\pi}{P}(t - t_0)\right]^2} \\ \partial_t p &= -\mathbf{w} \cdot \nabla p - \rho c^2(\nabla \cdot \mathbf{v} + Q), \end{aligned} \quad (51)$$

where $P = 100$ s is the dominant time period of the explosion and $t_0 = 75$ s is the starting time. The source is located at $x_S = 400$ km and $z_S = 400$ km. The atmosphere is again considered isothermal and described in Table 4.

Figure 4 shows that the waveform and the travel time are both computed accurately by the numerical simulation. We

| $L_x \times L_z$ (km) | Δx (m) | Δt (s) | ρ | c | η_V | μ | g_z | w_x |
|-----------------------|----------------|----------------|---------|--------|-----------|-------|--------|-------|
| 20×800 | 250 | 10^{-2} | varying | 652.82 | 10^{-4} | 0 | -9.831 | 0 |

Table 3. Simulation parameters corresponding to the full isothermal model 3.1 for Simulation 5.3, i.e., the case of a Bottom “high-frequency” forcing in an attenuating, windless atmosphere with exponentially-decaying density. In this table we express parameters with the following dimensions: ρ (kg.m⁻³), c (m.s⁻¹), η_V (kg.m⁻¹.s⁻¹), μ (kg.m⁻¹.s⁻¹), g_z (m.s⁻²) and w_x (m.s⁻¹).

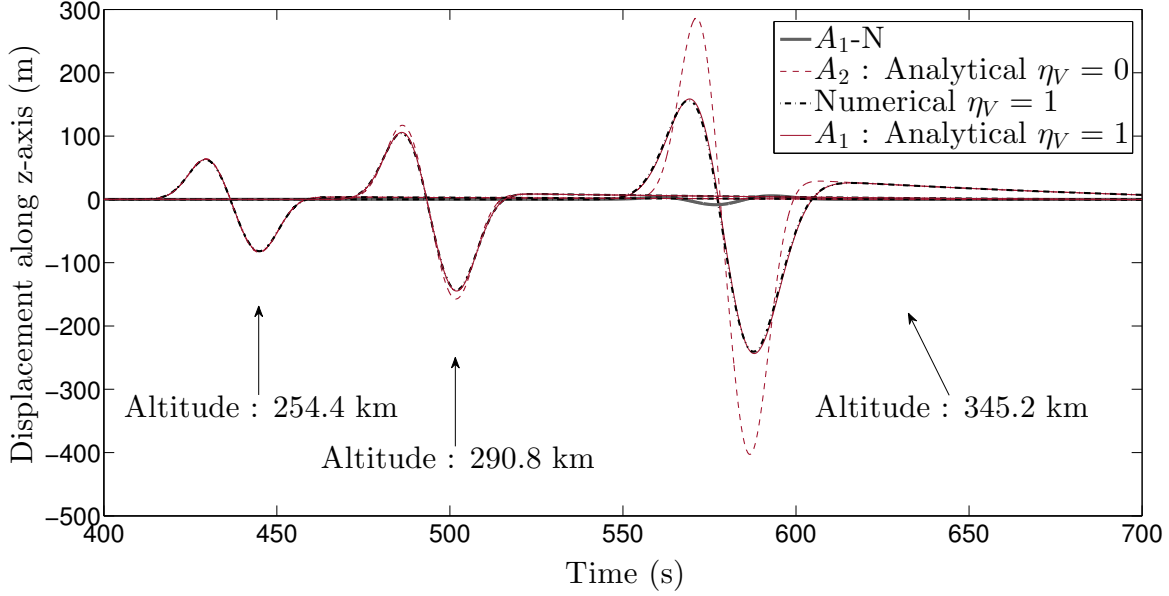


Figure 3. Vertical displacement for the finite-difference solution (‘Numerical’) and the analytical solution (‘Analytical A_1 ’) as well as the difference between the two (‘ A_1 -N’); we also show the case without viscosity (‘Analytical A_2 ’). The signals are shown through time for Simulation 5.3, i.e., the case of a Bottom “high-frequency” forcing in an attenuating, windless atmosphere with exponentially-decaying density, and for three recording stations located at altitudes $z = 2544$, 290.8 and 345.2 km. The atmosphere is considered isothermal (Table 3).

have scaled the source amplitude A in (B.2) to that recorded at the first station in the far field because the analytical solution (B.3) is valid only in the far-field domain. Several aspects of spherical acoustic waves propagation in a moving medium can be noticed. As expected the amplitude decreases as $1/\sqrt{r}$ in terms of geometrical spreading, compared to $1/r$ in a 3D medium, because this simulation is 2D. The Doppler shift due to wind is noticed through the frequency shift and amplitude variations between upwind and downwind acoustic propagation. As expected (Nappo 2002), upwind waves have larger periods and amplitudes than downwind ones.

6 2D GRAVITY WAVES

6.1 Bottom “low-frequency” forcing in an atmosphere with exponentially-decaying density

In order to study and validate gravito-acoustic wave propagation and the underlying physical processes, we consider the forcing function, $\forall \mathbf{x} \in \Gamma_{FS}$:

$$f(\mathbf{x}, t) = (e^{-[\frac{t-(t_0-P/4)}{P/4}]^2} - e^{-[\frac{t-(t_0+P/4)}{P/4}]^2})(e^{-\frac{x-(x_0-S/4)^2}{S/4}} - e^{-\frac{x-(x_0+S/4)^2}{S/4}}), \quad (52)$$

where $P = 1600$ s is the dominant time period of the forcing signal, $S = 80$ km is the dominant spatial period along x , $t_0 = 1400$ s is the starting forcing time, and $x_0 = 600$ km is the position of the bottom forcing along x . The atmosphere is considered isothermal and described in Table 5.

We will now compare numerical and analytical particle displacement at several recording stations. In this case station locations must be chosen wisely because internal gravity waves do not propagate in all directions. Indeed, the dispersion relation (B.4) without wind i.e. with $w_x = 0$ yields the angle of propagation β

$$\cos \beta = \frac{\omega}{N}, \quad (53)$$

| $L_x \times L_z (km)$ | $\Delta x (km)$ | $\Delta t (s)$ | ρ | c | η_V | μ | g_z | w_x |
|-----------------------|-----------------|----------------|--------|--------|----------|-------|--------|-------|
| 800×800 | 500 | 10^{-2} | 1.2 | 652.82 | 0 | 0 | -9.831 | 150 |

Table 4. Simulation parameters corresponding to the homogeneous isothermal model 3.1 for Simulation 5.4, i.e., the case of an Atmospheric explosion in a windy homogeneous atmosphere. In this table we express parameters with the following dimensions: ρ (kg.m^{-3}), c (m.s^{-1}), η_V ($\text{kg.m}^{-1}.\text{s}^{-1}$), μ ($\text{kg.m}^{-1}.\text{s}^{-1}$), g_z (m.s^{-2}) and w_x (m.s^{-1}).

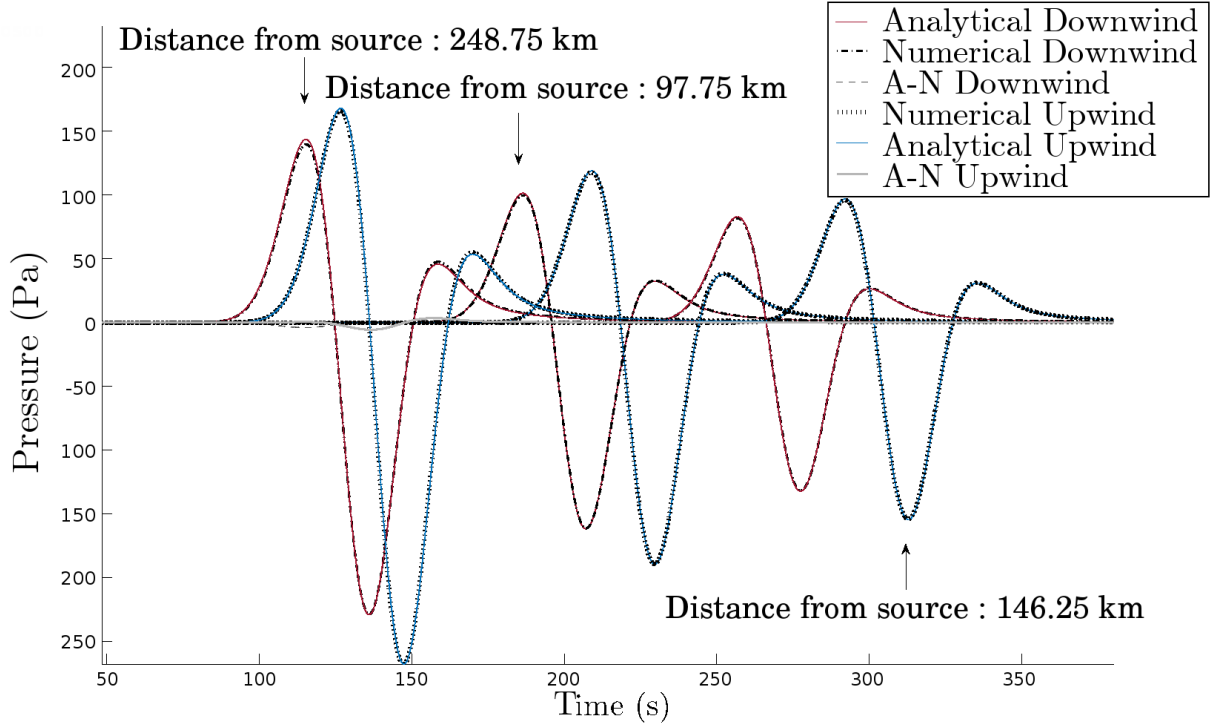


Figure 4. Pressure for the finite-difference upwind and downwind solutions (‘Numerical’) and the analytical upwind and downwind solutions (‘Analytical’) as well as the difference between the two upwind and downwind solutions (‘A-N’). The signals are shown through time for Simulation 5.4 , i.e., the case of an Atmospheric explosion in a windy homogeneous atmosphere, at six recording stations (three downwind and three upwind) located at altitude $z = z_S = 400$ km and at distances $x = 48.75, 97.75$ and 146.25 km away from the source. The atmosphere is considered isothermal (Table 4).

where N is the Brunt-Väisälä frequency and β is the angle between the horizontal axis x and the wave vector \mathbf{k} , such that

$$\mathbf{k} = |\mathbf{k}|(\cos \beta \mathbf{e}_x + \sin \beta \mathbf{e}_z). \quad (54)$$

We thus only select stations at positions for which $\beta_{stat} < \beta$, where β_{stat} is the angle between the horizontal axis x and the position vector of the station.

In Figure 5 one can see low-frequency gravity waves propagating in the stratified atmosphere. The figure shows low amplitude errors and a good fit in terms of phase velocity.

6.2 Bottom ”low-frequency” forcing in a windy atmosphere with exponentially-decaying density

6.2.1 Comparison with analytical solution

In order to study and validate the impact of wind on gravity wave propagation we use the same forcing (52) as above, with parameters $P = 1600$ s, $S = 80$ km, $t_0 = 1400$ s and $x_0 = 800$ km. The atmosphere is considered isothermal and described in Table 6.

In Figure 6, as in the acoustic case of Figure 4, one can notice the impact of the Doppler shift on gravity wave propagation: upwind waves have a larger period and larger amplitude than downwind ones.

In Figure 7 we present snapshots of the simulation. A typical feature of gravity wave propagation can be observed: the group (V_g) and phase velocities (V_p) are orthogonal. The pictures also illustrate an interesting aspect of our numerical

| $L_x \times L_z$ (km) | Δx (m) | Δt (s) | ρ | c | η_V | μ | g_z | w_x |
|-----------------------|----------------|----------------|---------|--------|----------|-------|--------|-------|
| 1200×400 | 500 | 10^{-2} | varying | 652.82 | 0 | 0 | -9.831 | 0 |

Table 5. Simulation parameters corresponding to the isothermal model 3.1 for Simulation 6.1 , i.e., the case of a Bottom ”low-frequency” forcing in an atmosphere with exponentially-decaying density. In this table we express parameters with the following dimensions: ρ (kg.m⁻³), c (m.s⁻¹), η_V (kg.m⁻¹.s⁻¹), μ (kg.m⁻¹.s⁻¹), g_z (m.s⁻²) and w_x (m.s⁻¹).

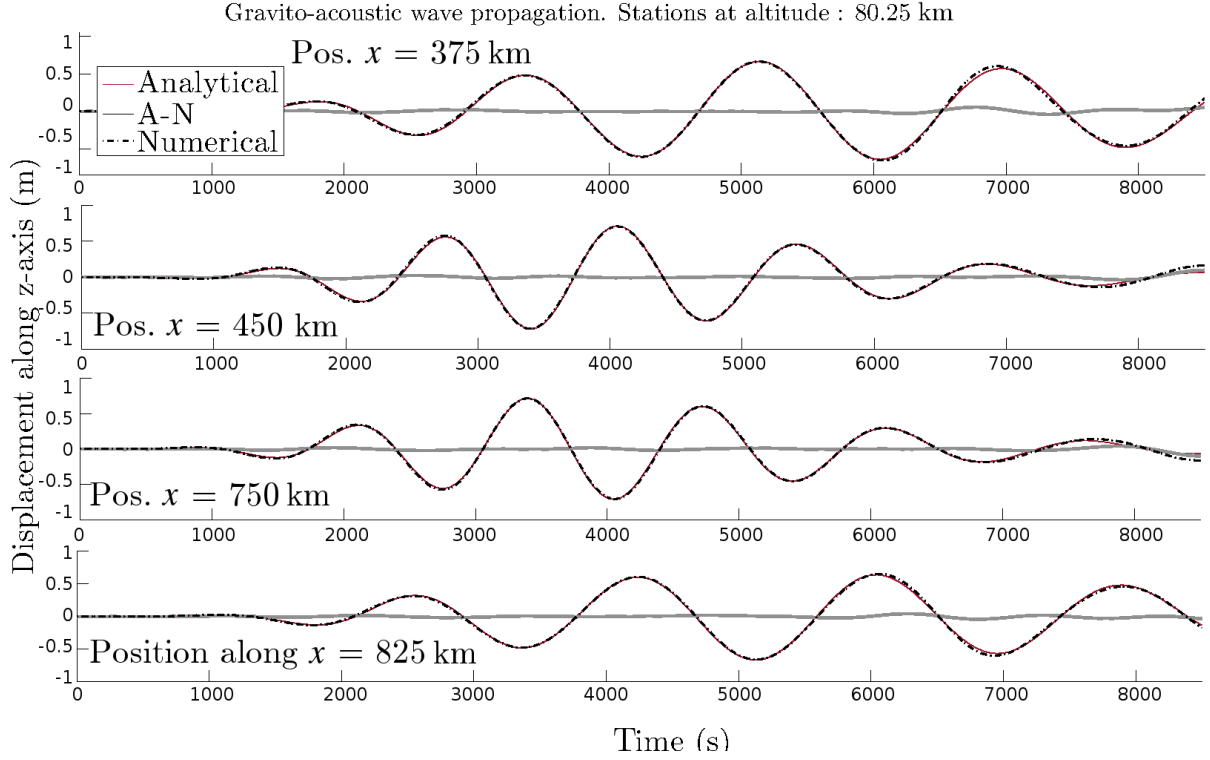


Figure 5. Vertical displacement for the finite-difference solution (‘Numerical’) and the analytical solution (‘Analytical’) as well as the difference between the two (‘A-N’). The signals are shown through time for Simulation 6.1, i.e., the case of a Bottom “low-frequency” forcing in an atmosphere with exponentially-decaying density, at the four recording stations located at the same altitude $z = 80.25$ km, their position along x being, from top to bottom, $x = 375, 450, 750$ and 825 km. The atmosphere is considered isothermal (Table 5).

modelling tool, which is that we can compute and show the propagation of gravity and acoustic waves simultaneously. One can thus notice an acoustic wave front propagating from the bottom to the top, ahead of gravity waves owing to the small positive amplitude of displacement perturbation u_z between the bottom forcing function (52) at t_1 and $t_1 + \Delta t$ such that $f(t_1) = 0; f(t_1 + \Delta t) > 0$. This step, similar to a Dirac, generates a high-frequency wave (an acoustic wave).

Note that in the comparisons presented in Figure 6 the impact of this “high-frequency” wave on the seismogram is not seen because its amplitude is tiny compared to that of the gravity wave.

6.2.2 Resolution analysis

In order to see the impact of resolution (spatial and time steps) on the displacement amplitude error, and since we have not performed any rigorous mathematical stability and accuracy analysis of the problem, we perform tests with various resolutions in the case of gravity waves propagating in a windy atmosphere.

We use a similar bottom forcing as in eq. (52), with parameters $P = 800$ s, $S = 25$ km, $t_0 = 800$ s and $x_0 = 250$ km and consider the atmosphere model specified in Table 7. In Figure 8, the left and right panels show how spatial resolution impacts the amplitude error through time. First, as one decreases the spatial step one can see that the error decreases, in particular for the largest error peaks (i.e. between $t = 2000$ s and $t = 3000$ s in the left panel). Owing to the cumulative nature of such

| $L_x \times L_z$ (km) | Δx (m) | Δt (s) | ρ | c | η_V | μ | g_z | w_x |
|-----------------------|----------------|----------------|---------|--------|----------|-------|--------|-------|
| 1600×400 | 500 | 10^{-2} | varying | 652.82 | 0 | 0 | -9.831 | 10 |

Table 6. Simulation parameters corresponding to the isothermal model 3.1 subject to wind for Simulation 6.2.1, i.e., the case of a Comparison with analytical solution. In this table we express parameters with the following dimensions: ρ (kg.m^{-3}), c (m.s^{-1}), η_V ($\text{kg.m}^{-1}.\text{s}^{-1}$), μ ($\text{kg.m}^{-1}.\text{s}^{-1}$), g_z (m.s^{-2}) and w_x (m.s^{-1}).

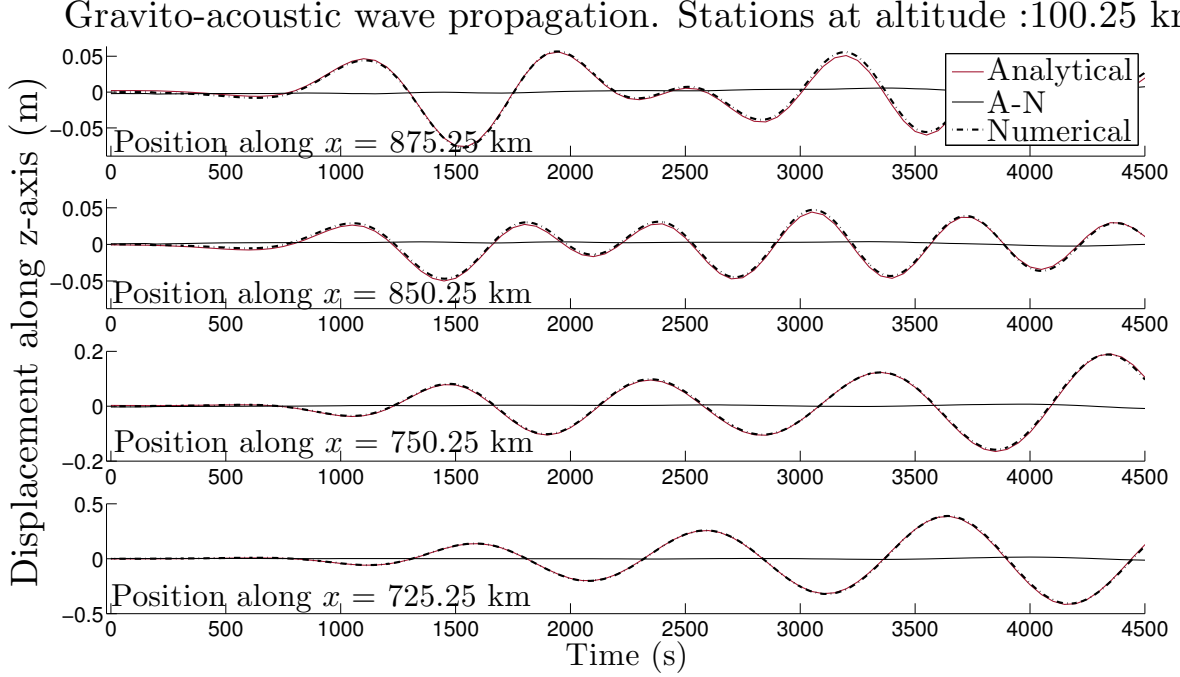


Figure 6. Vertical displacement for the finite-difference numerical solution ('Numerical') and the analytical solution ('Analytical') as well as the difference between the two ('A-N'). The signal is shown through time for Simulation 6.2.1, i.e., the case of a Comparison with analytical solution, at four recording stations located at the same altitude $z = 100.25$ km and whose position along x is, from top to bottom, $x = 875.25, 850.25, 750.25$ and 725.25 km. The atmosphere is considered isothermal (Table 6).

numerical error with time, accuracy is more impacted for long time periods than at the beginning of the simulation, where the error is similar for all spatial resolutions considered. At time $t = 2000$ s in the bottom-left chart one notices that the simulation with a larger spatial step exhibits lower error, but only temporarily. The "averaging" implied by a large spatial step $\Delta x = 1000$ m seems to, surprisingly, reproduce the phase of the analytical signal well, but as one decreases Δx the error gets lower than that for $\Delta x = 1000$ m. In the right panel the difference in displacement amplitude between simulations with resolution $\Delta x = 125$ m and $\Delta x = 250$ m shows that for this set of parameters (Table 7) the solution seems to be converging. If one decreases the time step Δt for the resolution $\Delta x = 125$ m one notices an improvement in accuracy at the beginning of the simulation, but after 1600 s both simulations give a similar result. With this resolution ($\Delta x = 125$ m and $\Delta t = 0.01$ s) the numerical solution has converged and decreasing the time step will not decrease the error any longer.

Another source of error comes from the numerical computation of the analytical solution. Indeed, a numerical Fourier transform and then a numerical inverse Fourier transform are required to compute the solution (refer to Section 5.1), which introduces numerical approximations. In Figure 9, we show the absolute error between numerical evaluations of the analytical solution computed with various resolutions. The resolution impacts directly the Fourier transform since it leads to a lower boundary (specified by the Nyquist frequency) for the number of points required, in order to overcome aliasing, in both spatial and time Fourier transforms. Thus, in the chart one notices that the number of spatial points has a significant impact on the analytical signal: one obtains almost a 5% difference in absolute amplitude between the signal computed for $\Delta x = 125$ m and for $\Delta x = 500$ m. The very small difference (about 10^{-14} m) obtained between spatial resolutions $\Delta x = 125$ m and $\Delta x = 250$ m shows that the solution has converged and then captured low vertical wavelength values.

This illustrates the fact that small errors sometimes observed in the validation cases presented in this work can be

| $L_x \times L_z$ (km) | Δx (m) | Δt (s) | ρ | c | η_V | μ | g_z | w_x |
|-----------------------|----------------|----------------|---------|--------|----------|-------|--------|-------|
| 1600×400 | 500 | 10^{-2} | varying | 652.82 | 0 | 0 | -9.831 | 10 |

Table 7. Simulation parameters corresponding to the isothermal model 3.1 subject to wind for Simulation 6.2.2, i.e., the case of a Resolution analysis. In this table we express parameters with the following dimensions: ρ (kg.m^{-3}), c (m.s^{-1}), η_V ($\text{kg.m}^{-1}.\text{s}^{-1}$), μ ($\text{kg.m}^{-1}.\text{s}^{-1}$), g_z (m.s^{-2}) and w_x (m.s^{-1}).

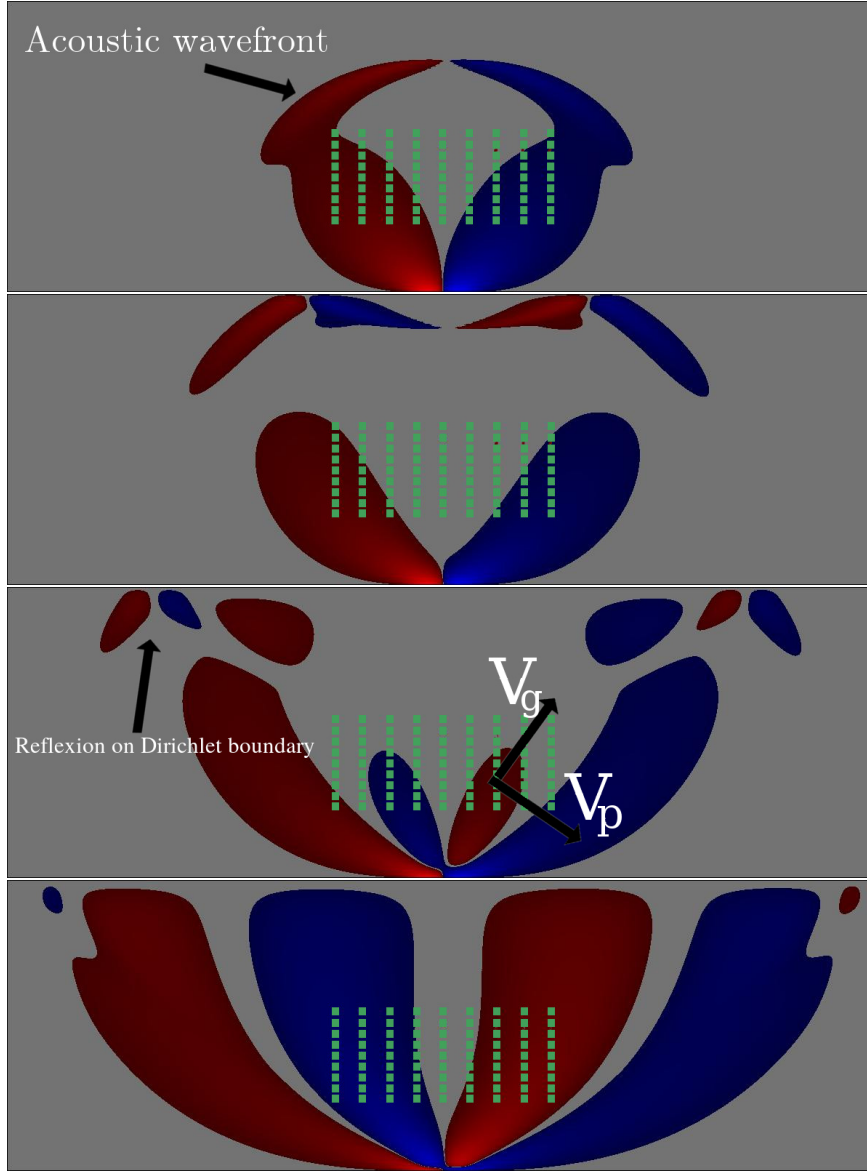


Figure 7. Vertical displacement for the finite-difference numerical solution for Simulation 6.2.1, i.e., the case of a Comparison with analytical solution. Red indicates positive vertical displacements and blue negative ones. The green squares show the location of the recording stations. Snapshots are taken, from top to bottom, at times $t = 500$ s, $t = 700$ s, $t = 900$ s and $t = 1100$ s. The origin of the coordinate system is at the bottom left of the domain. The atmosphere is considered isothermal (Table 6). A small acoustic wavefront is also observed. Phase and group velocities are indicated by V_p and V_g respectively in the third snapshot from the top, and are orthogonal.

explained by the resolution used in these simulations. If we had chosen smaller spatial steps for the numerical and analytical computations we could have decreased the error in phase and amplitude but the computation time would have thus significantly increased. As often with numerical schemes there is a tradeoff to find between accuracy and numerical cost.

7 2D APPLICATIONS

7.1 Bottom "low-frequency" forcing in an isothermal atmosphere subject to a wind duct

In this case we set up a wind duct (a strong wind velocity gradient) to show specific gravity-wave features studied by several authors (Ding et al. 2003; Nappo 2002). We use the same type of forcing as in Simulation 6.1, with parameters $P = 2800$ s, $S = 80$ km, $t_0 = 1600$ s and $x_0 = 1280$ km. The atmosphere is considered isothermal and described in Table 8.

In this case the wind profile is a wind duct, i.e a Gaussian bump such that

$$w_x(z) = 10 + w_{x,0} e^{-\left(\frac{z-\bar{z}}{\sigma}\right)^2} \quad (55)$$

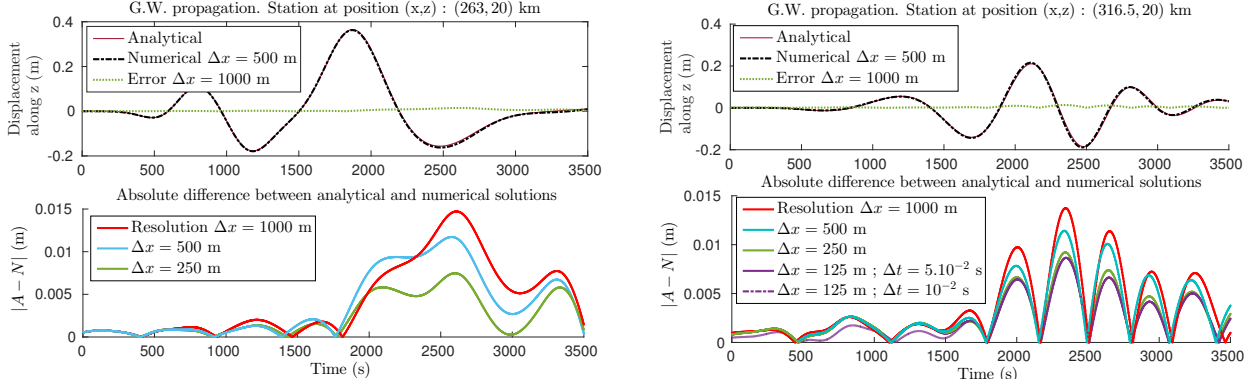


Figure 8. In the top charts, vertical displacement for the finite-difference solution (‘Numerical’) and the analytical solution (‘Analytical’) in case of a spatial step $\Delta x = 500$ m, as well as the difference between the two cases (‘Error’) for a spatial step $\Delta x = 1000$ m. The signals are shown through time for Simulation 6.2.2 at two recording stations located at the same altitude $z = 20$ km, their position along x being, from left to right, $x = 263$ and 316.5 km. The atmosphere is considered isothermal (Table 7). In the bottom charts we display amplitude through time of the absolute difference of vertical displacement between the analytical signal and the numerical one for various spatial steps $\Delta x = 125, 250, 500, 1000$ m and also for $\Delta t = 0.01$ s for the spatial resolution $\Delta x = 125$ m. For both stations, the amplitude of the error decreases with increasing resolution, as expected.

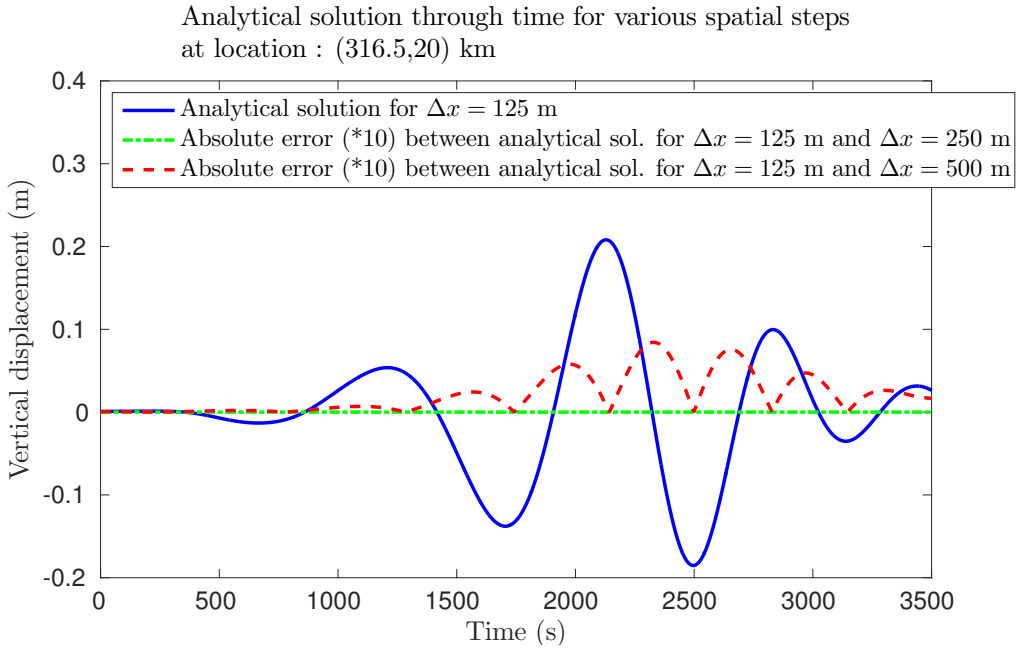


Figure 9. Vertical displacement for the analytical solution (‘Analytical solution’) in case of a spatial step $\Delta x = 125$ m, and amplitude through time of the absolute difference in vertical displacement (‘Absolute error’) between the analytical signals for various spatial steps: between signals for $\Delta x = 125$ and $\Delta x = 250$ m and also between signals for $\Delta x = 125$ and $\Delta x = 500$ m. Absolute amplitude errors are multiplied by 10 here in order to be able to see both in each chart. The signals are shown through time for Simulation 6.2.2, at the same recording station located at altitude $z = 20$ km and $x = 316.5$ km. The atmosphere is considered isothermal (Table 7). Errors decrease significantly as one increases the number of points used in the calculation of the numerical Fourier transform. The results also show that for $\Delta x = 250$ m the numerical calculation of the analytical solution has also converged.

| $L_x \times L_z$ (km) | Δx (m) | Δt (s) | ρ | c | η_V | μ | g_z | w_x |
|-----------------------|----------------|----------------|---------|--------|----------|-------|--------|-------|
| 2560×450 | 1000 | 10^{-2} | varying | 652.82 | 0 | 0 | -9.831 | var |

Table 8. Simulation parameters corresponding to the isothermal model 3.1 subject to wind for Simulation 7.1, i.e., the case of a Bottom “low-frequency” forcing in an isothermal atmosphere subject to a wind duct. In this table we express parameters with the following dimensions: ρ (kg.m^{-3}), c (m.s^{-1}), η_V ($\text{kg.m}^{-1}.\text{s}^{-1}$), μ ($\text{kg.m}^{-1}.\text{s}^{-1}$), g_z (m.s^{-2}) and w_x (m.s^{-1}).

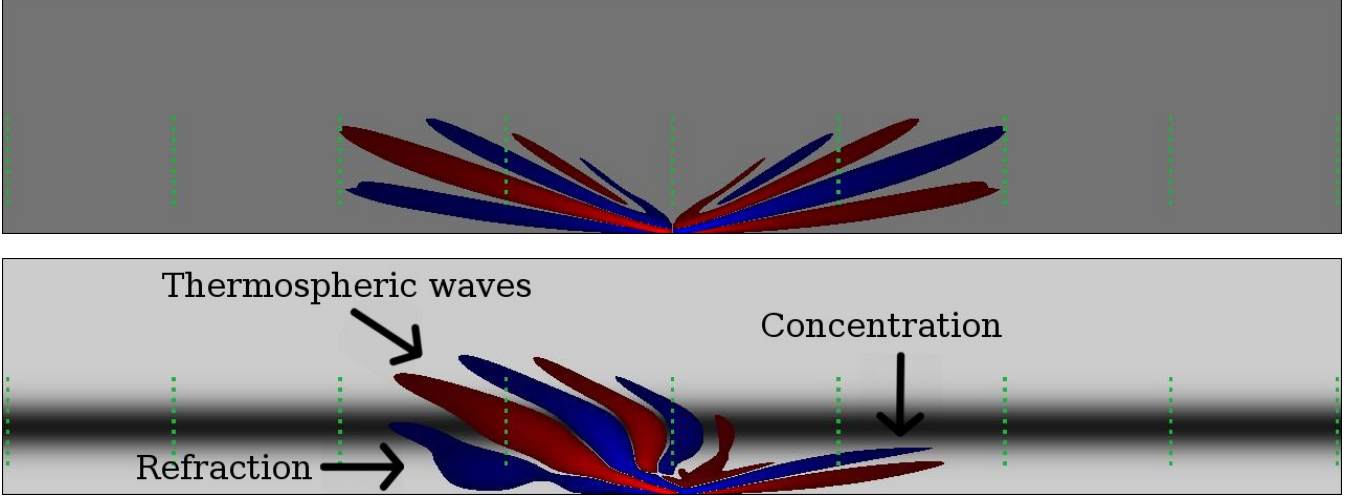


Figure 10. Normalized vertical displacement (the amplitude has been multiplied by $\sqrt{\rho}$ for visualization purposes) of the finite-difference numerical solution for the windless case (top) and the wind duct case (bottom) in Simulation 7.1, i.e., the case of a Bottom "low-frequency" forcing in an isothermal atmosphere subject to a wind duct. Both snapshots are taken at time $t = 2850$ s. Red indicates positive vertical displacements and blue negative ones. The green squares show the location of the recording stations. The origin of the coordinate system is at the bottom left of the domain. The atmosphere is considered isothermal (Table 8).

with $w_{x,0} = 200 \text{ m.s}^{-1}$, $\tilde{z} = 100 \text{ km}$ and $\sigma = 5000 \text{ m}$.

In Figure 10 three main features of gravity-wave propagation subject to a wind duct are seen: first, waves can go beyond the wave duct but the altitude reached by the upwind waves is much higher than the downwind ones. Second, some downwind waves seem to be concentrated around the wave duct. Finally, in the bottom left of the upwind waves, one can observe a refracted wave due to reflection on the wave duct owing to the strong wind velocity gradient.

7.2 Tsunami-like bottom forcing in a full MSISE based atmosphere

In this case let us consider the forcing function, $\forall \mathbf{x} \in \Gamma_F$,

$$f(\mathbf{x}, t) = (e^{-[\frac{t-(t_0-P/4)}{P/4}]^2} - e^{-[\frac{t-(t_0+P/4)}{P/4}]^2})(e^{-[\frac{x_0+v_t*t-(x_0-S/4)}{S/4}]^2} - e^{-[\frac{x-([x_0+v_t*t]+S/4)}{S/4}]^2}), \quad (56)$$

where $P = 800 \text{ s}$ is the dominant time period of the forcing signal, $S = 80 \text{ km}$ is the dominant spatial period along x of the forcing signal, $t_0 = 800 \text{ s}$ is the starting forcing time and $x_0 = 266.5 \text{ km}$ is the position of the bottom forcing along x . The tsunami wave velocity is $v_t = 100 \text{ m.s}^{-1}$. We define the atmosphere according to the MSISE-00 model described in Table 10.

In Figure 11, gravity waves propagate in a realistic atmosphere, which highlights the fact that simulations are stable in a relatively complex medium with strong gradients of the physical parameters. Waves coming from the right of the domain are due to the periodic boundary conditions implemented on the left and right boundaries. One can notice that gradients in sound and wind velocities (see Table 9) have a strong effect on the gravity wave curvature. Also, the Doppler shift is visible as one observes that the right part of the wavefront has a smaller apparent spatial period than the left part.

| $L_x \times L_z \text{ (km)}$ | $\Delta x \text{ (m)}$ | $\Delta t \text{ (s)}$ | ρ | c | η_V | μ | g_z | w_x |
|-------------------------------|------------------------|------------------------|---------|---------|----------|---------|---------|---------|
| 1600×400 | 500 | 10^{-3} | varying | varying | varying | varying | varying | varying |

Table 9. Simulation parameters corresponding to the MSISE model 3.2 subject to wind for Simulation 7.2, i.e., the case of a Tsunami-like bottom forcing in a full MSISE based atmosphere. In this table we express parameters with the following dimensions: $\rho \text{ (kg.m}^{-3}\text{)}$, $c \text{ (m.s}^{-1}\text{)}$, $\eta_V \text{ (kg.m}^{-1}\text{.s}^{-1}\text{)}$, $\mu \text{ (kg.m}^{-1}\text{.s}^{-1}\text{)}$, $g_z \text{ (m.s}^{-2}\text{)}$ and $w_x \text{ (m.s}^{-1}\text{)}$.

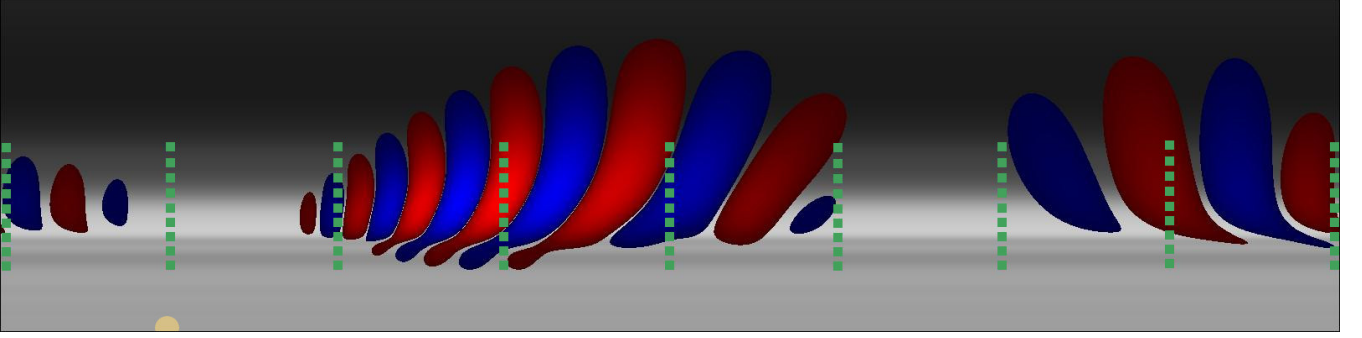


Figure 11. Vertical displacement for the finite-difference numerical solution for Simulation 7.2 , i.e., the case of a Tsunami-like bottom forcing in a full MSISE based atmosphere. Red indicates positive vertical displacements and blue negative ones. Background gray shades display variations with altitude of the horizontal wind velocity, white being the minimum value and black/dark gray the maximum value of the wind velocity described in Section 3.2. The green squares show the location of the recording stations. The yellow circle at the bottom left of the domain indicates the position x_0 of the forcing at time $t = 0$ s. The snapshot is taken at time $t = 2400$ s. The origin of the coordinate system is at the bottom left of the domain. The atmosphere model is based on *MSISE-00* (Table 9).

7.3 Seismic-like bottom forcing in a full MSISE based atmosphere

In this case we implement a large bottom x -velocity forcing v_t and a dominant time period P smaller than in the previous Simulation 56, such that, $\forall \mathbf{x} \in \Gamma_F$,

$$\begin{cases} f(\mathbf{x}, t) = e^{-\left[\frac{t-(t_0-P/2)}{P/2}\right]^2} \left(e^{-\left[\frac{x_0+v_t*t-(x_0-S/4)}{S/4}\right]^2} - e^{-\left[\frac{x-((x_0+v_t*t)+S/4)}{S/4}\right]^2} \right) & \text{if } t \leq t_0 - P/2, \\ f(\mathbf{x}, t) = e^{-\left[\frac{x_0+v_t*t-(x_0-S/4)}{S/4}\right]^2} - e^{-\left[\frac{x-((x_0+v_t*t)+S/4)}{S/4}\right]^2} & \text{if } t > t_0 - P/2 \end{cases} \quad (57)$$

with $P = 60$ s, $t_0 = 200$ s, $S = 320$ km, $x_0 = 266.5$ km, and $v_t = 4000$ m.s $^{-1}$. We define the atmosphere according to the MSISE-00 model described in Table 10.

In Figure 12 one can notice that the large ground forcing velocity v_t (see (57)) has a strong impact on the direction of wave propagation. We obtain almost horizontal wave fronts that can propagate in the upper atmosphere, with their trajectory impacted by wind and sound velocity gradients. The curvature of the wavefront in the thermosphere is due to the sudden increase of sound velocity.

7.4 Atmospheric explosion in a full MSISE based atmosphere

In this simulation we consider the same source as in Simulation 5.4 but with parameters $P = 20$ s as the dominant time period of the explosion and $t_0 = 50$ s as its starting time. The source Q is located at $x_S = 500$ km and $z_S = 100$ km. We define the atmosphere according to the MSISE-00 model described in Table 11.

In Simulation 7.4 (Figure 13), one can notice that a point source with a small dominant time period compared to the gravity wave frequency still generates both acoustic and gravity waves in the atmosphere, the latter propagating around the source location only, as predicted by observations and theory (Ben-Menahem & Singh 2012). Gravity waves are seen as this "low-frequency" oscillating signal that follows the acoustic wave front and that has a similar shape as in the gravity-wave Simulation 6.1. Once again one can observe the impact of wind that shifts the frequency spectrum of the gravity wave. Finally, when wind and sound velocity gradients are present they lead to atmospheric waveguides that impose a direction of propagation for acoustic and gravity waves.

| $L_x \times L_z$ (km) | Δx (m) | Δt (s) | ρ | c | η_V | μ | g_z | w_x |
|-----------------------|----------------|----------------|---------|---------|----------|---------|---------|---------|
| 1000 \times 400 | 500 | 10 $^{-3}$ | varying | varying | varying | varying | varying | varying |

Table 10. Simulation parameters corresponding to the MSISE model 3.2 subject to wind for Simulation 7.3 , i.e., the case of a Seismic-like bottom forcing in a full MSISE based atmosphere. In this table we express parameters with the following dimensions: ρ (kg.m $^{-3}$), c (m.s $^{-1}$), η_V (kg.m $^{-1}$.s $^{-1}$), μ (kg.m $^{-1}$.s $^{-1}$), g_z (m.s $^{-2}$) and w_x (m.s $^{-1}$).

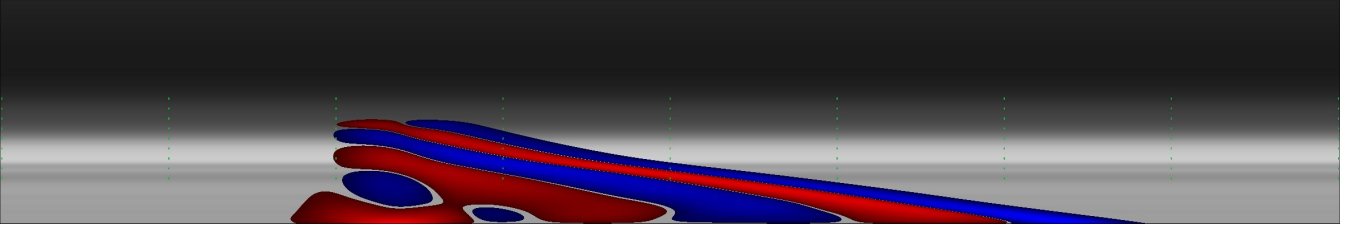


Figure 12. Vertical displacement for the finite-difference numerical solution. Red indicates positive vertical displacements and blue negative ones. The background gray shades indicate variations with altitude of the horizontal wind velocity, white being the minimum value and black/dark gray the maximum value of the wind velocity described in Section 3.2. The green squares show the location of the recording stations. The snapshot is taken at time $t = 680$ s. The origin of the coordinate system is at the bottom left of the domain. The atmosphere model is based on *MSISE-00* (Table 10).

| $L_x \times L_z$ (km) | Δx (m) | Δt (s) | ρ | c | η_V | μ | g_z | w_x |
|-----------------------|----------------|----------------|---------|---------|----------|---------|---------|---------|
| 4000×400 | 400 | 10^{-3} | varying | varying | varying | varying | varying | varying |

Table 11. Simulation parameters corresponding to the MSISE model 3.2 subject to wind for Simulation 7.4, i.e., the case of a Atmospheric explosion in a full MSISE based atmosphere. In this table we express parameters with the following dimensions: ρ (kg.m^{-3}), c (m.s^{-1}), η_V ($\text{kg.m}^{-1}.\text{s}^{-1}$), μ ($\text{kg.m}^{-1}.\text{s}^{-1}$), g_z (m.s^{-2}) and w_x (m.s^{-1}).

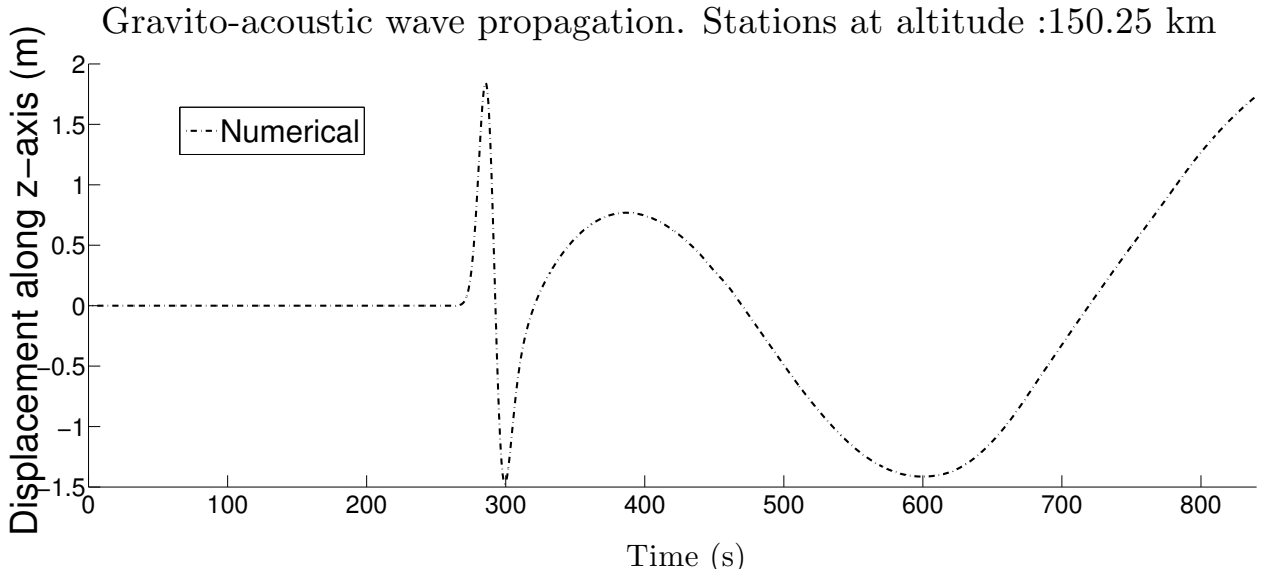
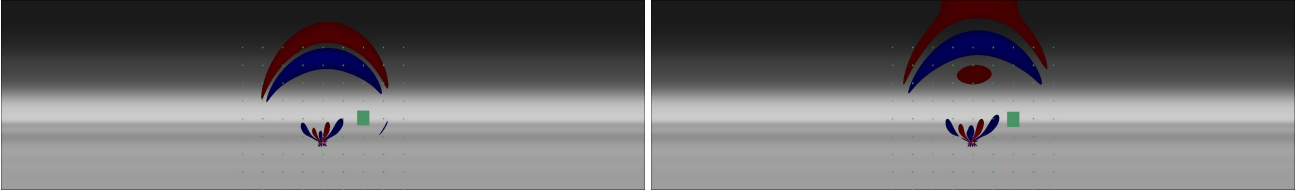


Figure 13. Vertical displacement for the numerical finite-difference solution at $t = 400$ s (left), $t = 450$ s (right) and over time at the station located at $x = 900.25\text{ km}$; $z = 150.25\text{ km}$ (bottom) for Simulation 7.4, i.e., the case of a Atmospheric explosion in a full MSISE based atmosphere. Red indicates positive vertical displacements and blue negative ones. The background gray shades indicate variations with altitude of the horizontal wind velocity, white being the minimum value and black/dark gray the maximum value of the wind velocity described in Section 3.2. The green squares show the location of the recording stations and the yellow cross is the source location. The origin of the coordinate system is at the bottom left of the domain. The atmosphere model is based on *MSISE-00* (Table 11).

| $L_x \times L_z$ (km) | Δx (m) | Δt (s) | ρ | c | η_V | μ | g_z | w_x |
|-----------------------------|----------------|----------------|--------|--------|----------|-------|-------|-------|
| $130 \times 130 \times 200$ | 500 | 10^{-2} | 1.2 | 652.82 | 0 | 0 | 0 | 0 |

Table 12. Simulation parameters corresponding to the isothermal model 3.1 not subject to wind for Simulation 8.1, i.e., the case of an Atmospheric explosion in a 3D homogeneous atmosphere. In this table we express parameters with the following dimensions: ρ (kg.m^{-3}), c (m.s^{-1}), η_V ($\text{kg.m}^{-1}.\text{s}^{-1}$), μ ($\text{kg.m}^{-1}.\text{s}^{-1}$), g_z (m.s^{-2}) and w_x (m.s^{-1}).

8 3D VALIDATION

8.1 Atmospheric explosion in a 3D homogeneous atmosphere

We perform a validation test in the 3D case by checking the impact of geometrical attenuation due to a point source generating a spherical wave. The pressure pulse is the same as in the 2D Simulation 5.4 but with parameters $P = 30$ s and $t_0 = 25$ s. The source is located at $x_S = 65$ km, $y_S = 65$ km and $z_S = 100$ km. The atmosphere is considered isothermal and described in Table 12.

In Figure 14 the waveform and travel time accurately match the analytical solution in this simple case. The maximum error over time is around 2%. This could be further reduced by increasing the spatial resolution, at the expense of larger computational times. The analytical pressure solution is not the same as in Simulation 5.4 but rather described by equation (B.5). This comparison validates the geometrical spreading of acoustic waves in a 3D case.

8.2 Bottom 1D "low-frequency" forcing in a 3D windy atmosphere with exponentially-decaying density

To validate 3D gravity wave propagation, we first perform a test with a ground forcing identical to the 2D gravity Simulation 6.2.1, i.e., the case of a Comparison with analytical solution. By "1D" here we mean that the ground forcing function only depends on x . By using this ground forcing uniform along y in the 3D simulation one should retrieve the same signal as in the 2D case.

The atmosphere is considered isothermal and described in Table 13.

As expected, in Figure 15 we obtain a good fit in terms of amplitude and phase between the 2D analytical signal and the

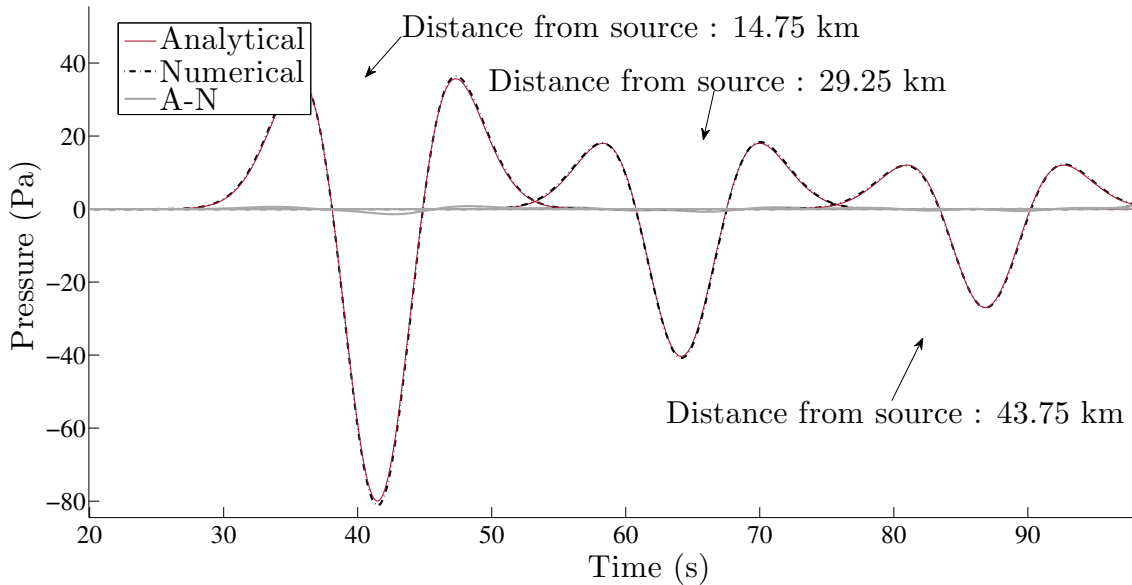


Figure 14. Pressure for the finite-difference numerical solution ('Numerical') and the analytical solution ('Analytical') as well as the difference between the two ('A-N'). The signals are shown through time for Simulation 8.1, i.e., the case of an Atmospheric explosion in a 3D homogeneous atmosphere, and for three recording stations located at altitude $z = z_S = 65$ km and at $y = y_S = 100$ km, and at distances $x = 14.75, 29.25,$ and 43.75 km away from the source. The atmosphere is considered isothermal (Table 12).

| $L_x \times L_y \times L_z$ (km) | Δx (m) | Δt (s) | ρ | c | η_V | μ | g_z | w_x |
|----------------------------------|----------------|----------------|---------|--------|----------|-------|--------|-------|
| $1600 \times 1600 \times 400$ | 5000 | 10^{-1} | varying | 652.82 | 0 | 0 | -9.831 | 10 |

Table 13. Simulation parameters corresponding to the isothermal model 3.1 subject to wind for Simulation 8.2 , i.e., the case of a Bottom 1D "low-frequency" forcing in a 3D windy atmosphere with exponentially-decaying density. In this table we express parameters with the following dimensions: ρ (kg.m⁻³), c (m.s⁻¹), η_V (kg.m⁻¹.s⁻¹), μ (kg.m⁻¹.s⁻¹), g_z (m.s⁻²) and w_x (m.s⁻¹).

3D numerical one. Results could be made even more accurate if one picked a smaller spatial step (identical to Simulation 6.2.1) Δx for numerical simulation.

8.3 Bottom 2D "low-frequency" forcing in a 3D windy atmosphere with exponentially-decaying density

In order to further validate 3D gravity wave propagation let us now use a similar approach than for the 2D gravity wave Simulation 6.2.1. Using a 2D ground forcing that depends on x and y in order to validate the propagation in the y direction. We will compare results to the analytical solution based on dispersion relation (B.4). Thus, in contrast to the 2D validation case we will perform a three dimensional Fourier Transform to take into account propagation in the (x, y) . We take a similar ground forcing as in Simulation 6.2.1 but convolved with a Gaussian that depends on x and y . We thus consider the following 3D forcing, $\forall \mathbf{x} \in \Gamma_{FS}$:

$$f(\mathbf{x}, t) = (e^{-[\frac{t-(t_0-P/4)}{P/4}]^2} - e^{-[\frac{t-(t_0+P/4)}{P/4}]^2})(e^{-[\frac{x-(x_0-S/4)}{S/4}]^2} - e^{-[\frac{x-(x_0+S/4)}{S/4}]^2})e^{-(\frac{d(\mathbf{x})}{S/4})^2}; \quad (58)$$

where $P = 1600$ s is the dominant time period of the forcing signal, $S = 80$ km is the dominant spatial period along x of the forcing signal, $t_0 = 1400$ s is the starting forcing time, $x_0 = y_0 = 500$ km is the position of the bottom forcing in the (x, y) plane and d is the distance from the point (x_0, y_0) such that $d(\mathbf{x}) = \sqrt{(x - x_0)^2 + (y - y_0)^2}$.

The atmosphere is considered isothermal and described in Table 14.

In Figure 16 one notices a good fit between the 3D numerical and 3D analytical signals in terms of phase and vertical displacement amplitude, with a maximum amplitude error of less than 5% over time. Geometrical spreading is visible since amplitudes in this case are smaller than in the previous validation case 6.2.1, i.e., the case of Bottom 2D "low-frequency" forcing in a 3D windy atmosphere with exponentially-decaying density. The Doppler effect also impacts gravity wave propagation: upwind waves have a larger period and larger amplitude than downwind ones.

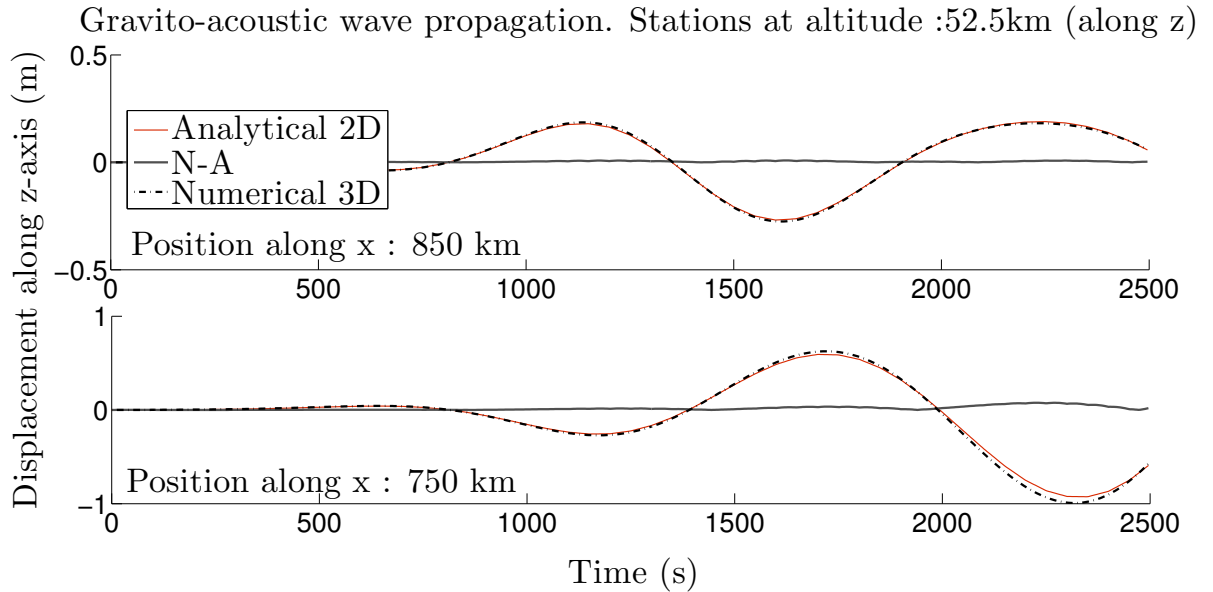


Figure 15. Vertical displacement for the 3D finite-difference numerical solution ('Numerical 3D'), and the 2D analytical solution ('Analytical 2D') as well as the difference between the 3D analytical signal and the 2D analytical one ('N - A'). Signals are shown through time for Simulation 8.2 , i.e., the case of a Bottom 1D "low-frequency" forcing in a 3D windy atmosphere with exponentially-decaying density, with uniform forcing along y (52) at two recording stations located at the same altitude $z = 52.5$ km and whose position along x is, from top to bottom, $x = 850$ and 750 km, and position along y is $y = 500$ km. The solid line in the bottom frame is the arrival time of both 2D and 3D gravity waves. The atmosphere is considered isothermal (Table 13).

| $L_x \times L_y \times L_z$ (km) | Δx (m) | Δt (s) | ρ | c | η_V | μ | g_z | w_x |
|----------------------------------|----------------|----------------|---------|--------|----------|-------|--------|-------|
| $1000 \times 1000 \times 400$ | 2500 | 5.10^{-2} | varying | 652.82 | 0 | 0 | -9.831 | 10 |

Table 14. Simulation parameters corresponding to the isothermal model 3.1 subject to wind for Simulation 8.3 , i.e., the case of a Bottom 2D "low-frequency" forcing in a 3D windy atmosphere with exponentially-decaying density. In this table we express parameters with the following dimensions: ρ (kg.m⁻³), c (m.s⁻¹), η_V (kg.m⁻¹.s⁻¹), μ (kg.m⁻¹.s⁻¹), g_z (m.s⁻²) and w_x (m.s⁻¹).

CONCLUSIONS AND FUTURE WORK

We have considered the linearized Navier-Stokes system of equations for acoustic and gravity wave propagation in a stratified and viscous moving medium. We have implemented a high-order finite-difference scheme that handles both acoustic and gravity waves simultaneously, in 2D or 3D media. We have also taken into account complex atmosphere models with strongly-varying wind and adiabatic sound velocities.

We validated the simulations by comparison to analytical solutions in several benchmark cases involving acoustic and gravity waves in a stratified windy and viscous atmosphere. We obtained very good agreement in terms of vertical displacement and pressure. The simulation results for validation cases exhibit interesting gravity wave characteristics and show the expected features: wave amplitude increases in vertical displacement with decrease of atmospheric density with altitude, and conversely wave amplitude tends to decrease with altitude due to viscosity, which mainly impacts high frequencies.

We also presented simulation results for an atmosphere model based on *MSISE-00* and for the cases of tsunami and seismic waves, and finally for an atmospheric explosion in the lower thermosphere. This showed that simulations are stable for complex media and exhibit interesting physical features such as change in wavefront curvatures with gradients in wind and sound velocities. Both acoustic and gravity waves propagate up to the upper-atmosphere. But with strong gradients in sound and wind velocities one also observes wave refraction and wave concentration in the thermosphere. Finally, one notices that the Doppler shift of the wave frequency spectrum has a significant impact on wave shape and arrival times.

This new numerical modelling tool can thus give insights on gravity wave dynamics in the atmosphere and enable one to study real signals such as those recorded by the GOCE satellite. It can also provide benchmark solutions in complex cases (such as the *MSISE-00* empirical atmosphere model) for future numerical developments.

Future developments should include absorbing boundary conditions instead of non-realistic horizontal periodic conditions in order to properly model wave propagation in the upper atmosphere. The technique should also take into account topography because it has an impact on the generation and propagation of gravity waves. Finally, coupling with a solid Earth and an

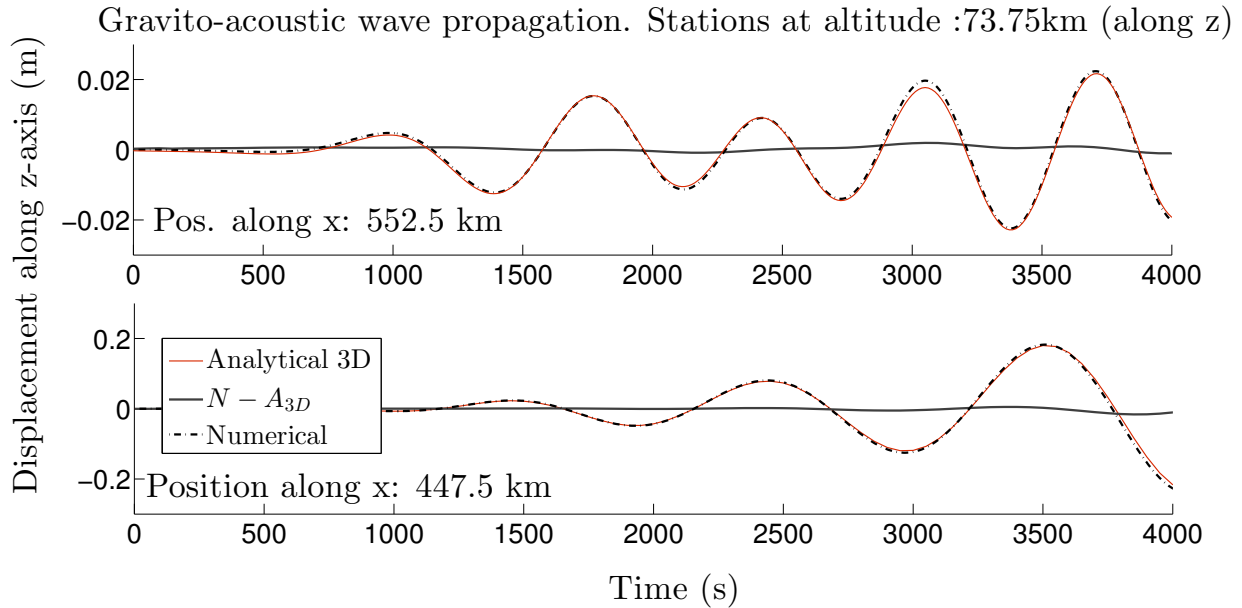


Figure 16. Vertical displacement for the 3D finite-difference numerical solution ('Numerical 3D') and the analytical 3D solution ('Analytical 3D') as well as the difference between the 3D numerical signal and the 3D analytical one (' $N - A_{3D}$ '). Signals are shown through time for Simulation 8.3 , i.e., the case of a Bottom 2D "low-frequency" forcing in a 3D windy atmosphere with exponentially-decaying density, at two recording stations located at the same altitude $z = 73.75$ km and whose position along x is, from top to bottom, $x = 552.5$ and 447.5 km, and position along y is $y = 500$ km. The atmosphere is considered isothermal (Table 14).

ocean should be implemented to better model the whole process from seismic underground perturbation to atmospheric wave propagation.

Acknowledgments

The authors thank Bruno Voisin for discussion about his work (Voisin 1994) and for giving them more details on the pressure response of an explosion in a moving medium. They are also grateful to Bernard Valette for mathematical discussion about the Euler equations. We acknowledge 2 anonymous reviewers for their constructive reviews improving this study. Computer resources were provided by granted projects no. p1138 at CALMIP computing centre (Toulouse France), nos. t2014046351 and t2015046351 at CEA centre (Bruyères, France). This work was also granted access to the French HPC resources of TGCC under allocations t2015-gen6351 and 2015-gen7165 made by GENCI. They also thank the "Région Midi-Pyrénées" (France) and "Université de Toulouse" for funding the Ph.D. grant of Quentin Brissaud. This study was also supported by CNES/TOSCA through space research scientific projects.

8.4 Appendices

APPENDIX A: EXPANSION OF THE MOMENTUM EQUATION IN COMPONENT FORM

Here let us give the component form of Eq. (24) that has been implemented into our finite-difference in the time domain (FDTD) code:

$$\begin{aligned}
 \partial_t p &= -(w_x \partial_x p + w_y \partial_y p) - \rho c^2 (\partial_x v_x + \partial_y v_y + \partial_z v_z) - \rho v_z g_z \\
 \partial_t \rho_p &= -(w_x \partial_x \rho_p + w_y \partial_y \rho_p) - \{\partial_x (\rho v_x) + \partial_y (\rho v_y) + \partial_z (\rho v_z)\} \\
 \rho \partial_t v_x &= -\rho (v_z \partial_z w_x + w_x \partial_x v_x + w_y \partial_y v_x) - \partial_x p \\
 &\quad + (\eta_V - \frac{2}{3}\mu) \partial_x \{(\partial_x v_x + \partial_y v_y + \partial_z v_z)\} \\
 &\quad + \mu [2\partial_x^2 \{v_x + w_x\} + \partial_y \{\partial_x v_y + \partial_y v_x\} \\
 &\quad + \partial_z \{\partial_x v_z + \partial_z (v_x + w_x)\}] \\
 \rho \partial_t v_y &= -\rho (v_z \partial_z w_y + w_x \partial_x v_y + w_y \partial_y v_y) - \partial_y p \\
 &\quad + (\eta_V - \frac{2}{3}\mu) \partial_y \{(\partial_x v_x + \partial_y v_y + \partial_z v_z)\} \\
 &\quad + \mu [\partial_x \{\partial_x v_y + \partial_y v_x\} + 2\partial_y^2 v_y \\
 &\quad + \partial_z \{\partial_y v_z + \partial_z (v_y + w_y)\}] \\
 \rho \partial_t v_z &= -\rho (w_x \partial_x v_z + w_y \partial_y v_z) - \partial_z p \\
 &\quad + \partial_z \{(\eta_V - \frac{2}{3}\mu) (\partial_x v_x + \partial_y v_y + \partial_z v_z)\} \\
 &\quad + \mu [\partial_x \{\partial_x v_z + \partial_z v_x\} + \partial_y \{\partial_y v_z + \partial_z v_y\} \\
 &\quad + 2\partial_z^2 v_z] \\
 &\quad + g_z \rho_p
 \end{aligned} \tag{A.1}$$

APPENDIX B: DISPERSION RELATIONS FOR THE VALIDATION CASES

The three validation cases presented above involve the following analytical formulation of the dispersion equations:

Acoustic wave forcing in a 2D heterogeneous windless atmosphere

The dispersion equation, without any source inside the domain and when one considers a windless atmosphere with varying density, sound velocity and viscosity (not considering shear viscosity), reads

$$k_z^2 (1 - \frac{i}{D}) - \frac{D}{H} k + \frac{1}{4H^2} (1 + \frac{i}{D}) - \left(\frac{\omega}{c}\right)^2 = 0, \tag{B.1}$$

where $D = \frac{\rho c^2}{\omega \eta_V}$.

Atmospheric explosion in 2D windy atmosphere

We consider a monochromatic point source Q that reads

$$\begin{aligned}
 Q &= \frac{2iA}{\rho\omega} e^{-i\omega t} \delta(x) \delta(z) \\
 \partial_t p &= -\mathbf{w} \cdot \nabla p - \rho c^2 (\nabla \cdot \mathbf{v} + Q),
 \end{aligned} \tag{B.2}$$

where A is the amplitude of the source pulse and δ the Kronecker symbol, from Ostashev et al. (2005), in the far-field approximation $k_x R \gg 1$, we get

$$\hat{p} = \frac{A(\sqrt{1 - M^2 \sin^2 \beta} - M \cos \beta)}{\sqrt{2\pi k R (1 - M^2)(1 - M^2 \sin^2 \beta)^{3/4}}} e^{\frac{i}{1 - M^2} (\sqrt{1 - M^2 \sin^2 \beta} - M \cos \beta) k R + \frac{i\pi}{4}}, \tag{B.3}$$

where $k = \frac{\omega}{c}$, M is the Mach number ($M = \frac{w}{c}$), β the angle between the x axis and the receiver and $R = \sqrt{(x - x_S)^2 + (z - z_S)^2}$ the source-receiver distance, with (x_S, z_S) the Cartesian coordinates of the source.

The theoretical pressure response for gravity waves for an explosion in a stratified windy atmosphere is more difficult to implement and can be found for instance in Voisin (1994) and Godin & Fuks (2012).

Gravity-wave forcing in a 3D stratified windy isothermal atmosphere

The dispersion equation, without any source inside the domain and when one considers a windy and inviscid atmosphere with varying density and sound velocity, reads

$$k_z^2 = \frac{(k_x^2 + k_y^2)N^2}{\Omega^2} - \frac{1}{4H^2} - k_x^2 - k_y^2, \quad (\text{B.4})$$

where k_x, k_y are the wavenumbers respectively along x and y , such that $k_x = \frac{2\pi}{\lambda_x}$ and $k_y = \frac{2\pi}{\lambda_y}$, λ_x, λ_y the wavelengths respectively along x and y , Ω is the intrinsic frequency such that $\Omega = \omega - w_x k_x - w_y k_y$, and H the scale height.

Atmospheric explosion in a 3D atmosphere

For a monochromatic point source \hat{Q} in a system following (B.2) from Goldstein (1976) one has

$$\hat{p} = \frac{A}{4\pi R} e^{ikR} \quad (\text{B.5})$$

where $k = \frac{\omega}{c}$ and $R = \sqrt{(x - x_S)^2 + (y - y_S)^2 + (z - z_S)^2}$ is the source-receiver distance, with (x_S, z_S) the Cartesian coordinates of the source. In this case no far-field assumption needs to be made because the full analytical solution is known in the whole domain.

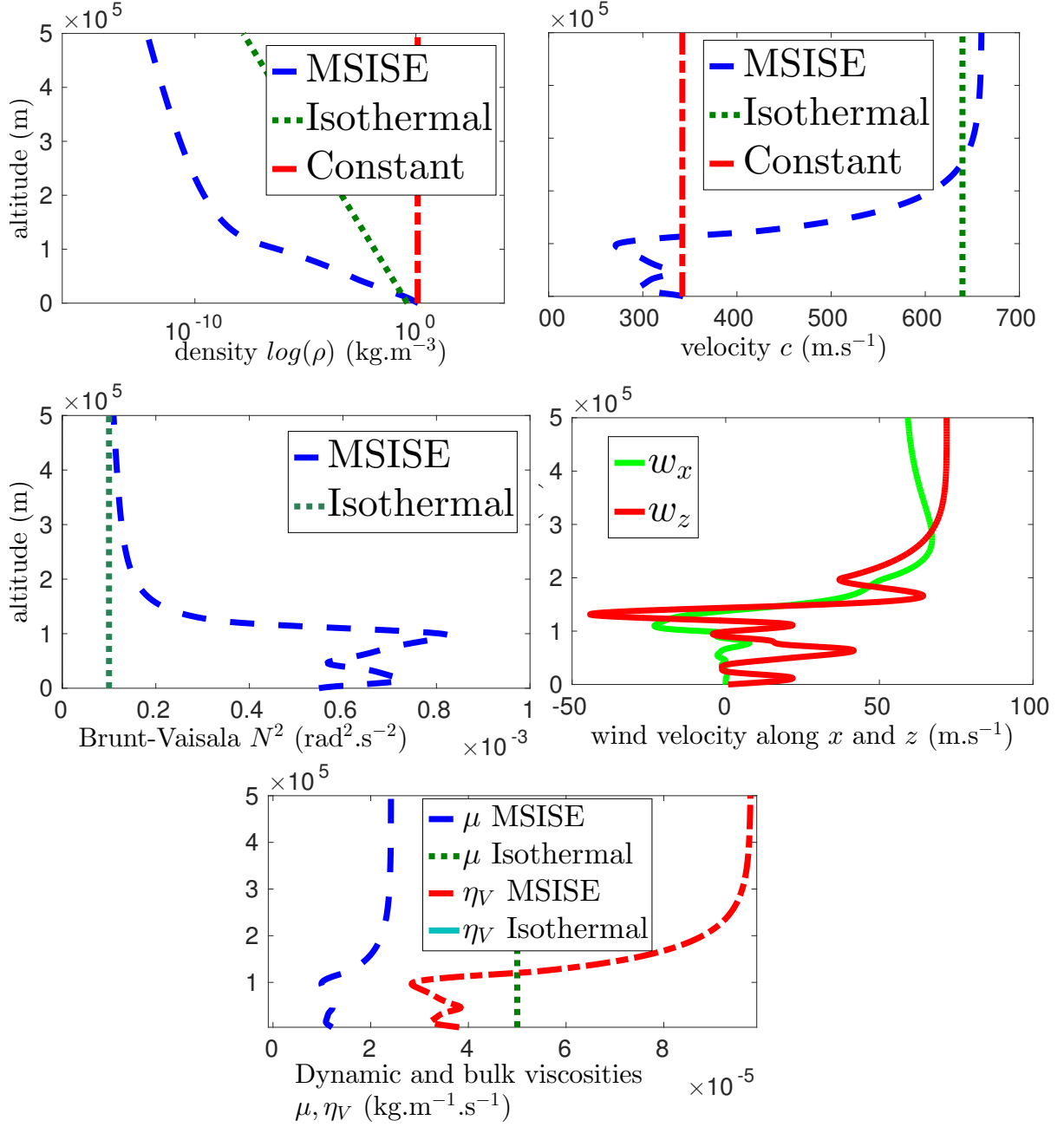


Figure A1. Vertical profiles extracted from the MSISE-00 atmosphere model and used for construction of the realistic atmosphere models in Section 3.2.

APPENDIX C: REALISTIC ATMOSPHERE MODEL

In figure A1 we present all the physical parameters plotted against altitude extracted from the MSISE-00 atmosphere model (Section 3.2).

APPENDIX D: VARIABLES

Table A1 summarizes all the variables used in the article. By "Total" in Table A1 we refer to the sum of the mean and fluctuating parts, see Hypothesis (iii).

Table A1. The main variables used in our article

| Name | Meaning | Name | Meaning |
|--------------------------------|-------------------------------------|--------------|---|
| \mathbf{u} | Displacement perturbation | c | Sound speed |
| \mathbf{v} | Velocity perturbation | ρ | Atmosphere mean density |
| $\mathbf{w} = (w_x, 0, 0)$ | Wind background velocity | ρ_p | Density perturbation |
| p | Pressure perturbation | η_V | Volume viscosity |
| \mathbf{I}_d | Identity tensor in \mathbb{R}^3 | μ | Dynamic viscosity |
| Σ | Eulerian stress tensor | \mathbf{g} | Gravitational acceleration |
| I | Internal energy | C_V | Heat capacity at constant volume |
| Q | Heat input | C_p | Heat capacity at constant pressure |
| T | Temperature | ρ_T | Total atmospheric density |
| \mathbf{U} | Total displacement | P | Total adiabatic atmospheric pressure |
| \mathbf{V} | Total velocity | \mathbf{G} | Total gravitational acceleration |
| \mathcal{F}_{ext} | External volumic forces | R | Gas constant |
| γ | Ratio of specific heat | L | Mean free path |
| κ | Thermal conductivity | α | Absorption coefficient |
| f, w | Frequency, Pulsation | Q | Quality factor |
| \mathbf{k} | Wavenumber | N | Brunt-Väisälä frequency |
| $\Delta x, \Delta y, \Delta z$ | Spatial step along x, y and z | Δt | Time step |
| L_x, L_y, L_z | Mesh dimension along x, y and z | β | Angle between the x axis and the receiver position |
| Γ_F | Forcing boundary | Γ_D | Dirichlet boundary |

REFERENCES

- Bass, H., Sutherland, L., Piercy, J., & Evans, L., 1984. Absorption of sound by the atmosphere, in *Physical acoustics: Principles and methods. Volume 17. Orlando, Florida, USA, Academic Press*, vol. 17, pp. 145–232.
- Bass, H. E. & Chambers, J. P., 2001. Absorption of sound in the Martian atmosphere, *J. Acoust. Soc. Am.*, **109**, 3069–3071.
- Ben-Menahem, A. & Singh, S. J., 2012. *Seismic waves and sources*, Springer Science & Business Media.
- Berland, J., Bogey, C., & Bailly, C., 2006. Low-dissipation and low-dispersion fourth-order Runge-Kutta algorithm, *Computers & Fluids*, **35**(10), 1459–1463.
- Blackstock, D. T., 2000. *Fundamentals of physical acoustics*, John Wiley & Sons.
- Carcione, J. M., 2014. *Wave fields in real media: Wave propagation in anisotropic, anelastic, porous and electromagnetic media*, Elsevier.
- Carcione, J. M., Kosloff, D., & Kosloff, R., 1988. Wave propagation simulation in a linear viscoelastic medium, *Geophysical Journal International*, **95**(3), 597–611.
- Chaljub, E., 2000. *Modélisation numérique de la propagation d'ondes sismiques en géométrie sphérique : application à la sismologie globale (Numerical modeling of the propagation of seismic waves in spherical geometry: application to global seismology)*, Ph.D. thesis, Université Paris VII Denis Diderot, Paris, France.
- Chaljub, E., Komatitsch, D., Vilotte, J.-P., Capdeville, Y., Valette, B., & Festa, G., 2007. Spectral-element analysis in seismology, *Advances in Geophysics*, **48**, 365–419.
- Coulouvrat, F., 2012. New equations for nonlinear acoustics in a low Mach number and weakly heterogeneous atmosphere, *Wave Motion*, **49**(1), 50 – 63.
- Cowling, T. G., 1941. The non-radial oscillations of polytropic stars, *Mon. Not. Roy. Astron. Soc.*, **101**, 369–373.
- de Groot-Hedlin, C., Hedlin, M. A. H., & Walker, K., 2011. Finite difference synthesis of infrasound propagation through a windy, viscous atmosphere: Application to a bolide explosion detected by seismic networks, *Geophysical Journal International*, **185**(1), 305–320.
- Ding, F., Wan, W., & Yuan, H., 2003. The influence of background winds and attenuation on the propagation of atmospheric gravity waves, *Journal of atmospheric and solar-terrestrial physics*, **65**(7), 857–869.
- Dörnbrack, A. & Nappo, C. J., 1997. A note on the application of linear wave theory at a critical level, *Boundary-Layer Meteorology*, **82**(3), 399–416.
- Ferziger, J. H. & Peric, M., 2012. *Computational methods for fluid dynamics*, Springer Science.
- Garcia, R. F., Drossart, P., Piccioni, G., López-Valverde, M., & Occhipinti, G., 2009. Gravity waves in the upper atmosphere of Venus revealed by CO₂ nonlocal thermodynamic equilibrium emissions, *Journal of Geophysical Research (Planets)*, **114**(E13), E00B32.
- Garcia, R. F., Bruinsma, S., Lognonné, P., Doornbos, E., & Cachoux, F., 2013. GOCE: The first seismometer in orbit around the Earth, *Geophys. Res. Lett.*, **40**, 1015–1020.
- Garcia, R. F., Doornbos, E., Bruinsma, S., & Hebert, H., 2014. Atmospheric gravity waves due to the Tohoku-Oki tsunami observed in the thermosphere by GOCE, *Journal of Geophysical Research (Atmospheres)*, **119**, 4498–4506.
- Godin, O. A., 2014. Dissipation of acoustic-gravity waves: An asymptotic approach, *Journal of the Acoustical Society of America*, **136**(6), EL411–EL417.
- Godin, O. A. & Fuks, I. M., 2012. Transmission of acoustic-gravity waves through gas–liquid interfaces, *Journal of Fluid Mechanics*, **709**, 313–340.
- Goldstein, M. E., 1976. *Aeroacoustics*, McGraw-Hill, New-York, USA.
- Graves, R. W., 1996. Simulating seismic wave propagation in 3D elastic media using staggered-grid finite differences, *Bull. Seismol. Soc. Am.*, **86**(4), 1091–1106.
- Gropp, W., Lusk, E., & Skjellum, A., 1994. *Using MPI, portable parallel programming with the Message-Passing Interface*, MIT Press, Cambridge, USA.
- Hedin, A., 1991. Extension of the MSIS thermosphere model into the middle and lower atmosphere, *J. Geophys. Res.*, **96**, 1159–1171.
- Hines, C. O., 1960. Internal atmospheric gravity waves at ionospheric heights, *Canadian Journal of Physics*, **38**, 1441.
- Kherani, E. A., Lognonné, P., Kamath, N., Crespon, F., & Garcia, R. F., 2009. Response of the ionosphere to the seismic triggered acoustic waves: electron density and electromagnetic fluctuations, *Geophysical Journal International*, **176**, 1–13.
- Landau, L. D. & Lifshitz, E. M., 1959. *Fluid mechanics*, Pergamon Press, New-York, USA.
- Le Pichon, A., Blanc, E., & Hauchecorne, A., 2010. *Infrasound monitoring for atmospheric studies*, Springer.
- Lecoanet, D., Le Bars, M., Burns, K. J., Vasil, G. M., Brown, B. P., Quataert, E., & Oishi, J. S., 2015. Numerical simulations of internal wave generation by convection in water, *Phys. Rev. E*, **91**, 063016.
- Lognonné, P., Clévédy, E., & Kanamori, H., 1998. Normal-mode summation of seismograms and barograms in a spherical earth with realistic atmosphere, *Geophys. J. Int.*, **135**, 388–406.
- Madariaga, R., 1976. Dynamics of an expanding circular fault, *Bull. Seismol. Soc. Am.*, **66**(3), 639–666.
- Makela, J. J., Lognonné, P., Hébert, H., Gehrels, T., Rolland, L., Allgeyer, S., Kherani, A., Occhipinti, G., Astafyeva, E., Coisson, P., Loevenbruck, A., Clévédy, E., Kelley, M. C., & Lamouroux, J., 2011. Imaging and modeling the ionospheric airglow response over Hawaii to the tsunami generated by the Tohoku earthquake of 11 March 2011, *Geophys. Res. Lett.*, **38**:L00G02(24).
- Mikhailenko, B. & Mikhailov, A., 2014. Numerical modeling of seismic and acoustic-gravity waves propagation in an earth-atmosphere model in the presence of wind in the air, *Numerical Analysis and Applications*, **7**(2), 124–135.
- Miyoshi, Y., Fujiwara, H., Jin, H., & Shinagawa, H., 2014. A global view of gravity waves in the thermosphere simulated by a general circulation model, *Journal of Geophysical Research: Space Physics*, **119**(7), 5807–5820.
- Moczo, P., 1989. Finite-difference technique for SH waves in 2-D media using irregular grids, application to the seismic response problem, *Geophys. J. Int.*, **99**, 321–329.
- Moczo, P. & Kristek, J., 2005. On the rheological models used for time-domain methods of seismic wave propagation, *Geophys. Res. Lett.*, **32**, L01306.
- Nappo, C., 2002. *An introduction to atmospheric gravity waves*, Academic Press.
- Occhipinti, G., Lognonné, P., Kherani, E., & Hébert, H., 2006. Three-dimensional waveform modeling of ionospheric signature induced by the 2004 Sumatra tsunami, *Geophys. Res. Lett.*, **33**, L20104, doi:10.1029/2006GL026865.

- Ostashev, V. E., Wilson, D. K., Liu, L., Aldridge, D. F., Symons, N. P., & Marlin, D., 2005. Equations for finite-difference, time-domain simulation of sound propagation in moving inhomogeneous media and numerical implementation, *Journal of the Acoustical Society of America*, **117**(2), 503–517.
- Picone, J. M., Hedin, A. E., Drob, D. P., & Aikin, A. C., 2002. NRLMSISE-00 empirical model of the atmosphere: Statistical comparisons and scientific issues, *Journal of Geophysical Research (Space Physics)*, **107**, 1468.
- Robertsson, J. O. A., Blanch, J. O., & Symes, W. W., 1994. Viscoelastic finite-difference modeling, *Geophysics*, **59**, 1444–1456.
- Snively, J. B. & Pasko, V. P., 2008. Excitation of ducted gravity waves in the lower thermosphere by tropospheric sources, *Journal of Geophysical Research: Space Physics*, **113**(A6), 6303.
- Valette, B., 1987. *Spectre des oscillations libres de la Terre: aspects mathématiques et géophysiques (Spectrum of the free oscillations of the Earth: mathematical and geophysical aspects)*, Ph.D. thesis, Université Paris VI Jussieu, Paris, thèse d'état.
- Vallis, G. K., 2006. *Atmospheric and oceanic fluid dynamics: fundamentals and large-scale circulation*, Cambridge University Press.
- Voisin, B., 1994. Internal wave generation in uniformly stratified fluids, Part 2: Moving point sources, *Journal of Fluid Mechanics*, **261**, 333–374.
- Wei, C., Bühler, O., & Tabak, E. G., 2015. Evolution of tsunami-induced internal acoustic-gravity waves, *Journal of the Atmospheric Sciences*, **72**(6), 2303–2317.
- Wilson, D. K., Symons, N. P., Patton, E. G., Ketcham, S. A., Andreas, E. L., & Collier, R. L., 2004. Simulation of sound propagation through high-resolution atmospheric boundary layer turbulence fields, in *Proceedings of AMS Symposium on Boundary Layers and Turbulence*, American Meteorological Society, CD-ROM P2.2, 6 pp.
- Yee, K. S., 1966. Numerical solution of initial boundary value problems involving Maxwell's equations, *IEEE Transactions on Antennas and Propagation*, **14**, 302–307.
- Zuckerwar, A. J. & Ash, R. L., 2006. Variational approach to the volume viscosity of fluids, *Physics of Fluids*, **18**(4), 047101.